National Technical University of Athens
Computational Mechanics Master Program
Fluids Section
School of Chemical Engineering

Computational study of crystal breakage with the Cell Average Technique

Master Thesis

Palatos Alexandros

Supervisor
Assistant Professor: Michalis Kavousanakis

Athens, 2022

Acknowledgments

First and foremost, I would like to express my gratitude to my supervisor, assistant professor Mihalis Kavousanakis who gave me the opportunity for collaboration in such an interesting project. The remarks and the advice he gave me were always very helpful and enlightening.

I would also like to acknowledge professor Georgios Stefanidis and Dr. Christos Xiouras for always being willing to provide help and knowledge.

Then, I would like to thank Dr. Antonis Spyropoulos who helped me to configure the necessary calculations in the cluster of Department of Process Analysis and Plant Design.

Last but not least, I would like to thank my family and my friends for every kind of support they provide.

National Technical University of Athens
Computational Mechanics Master Program
Fluids Section
School of Chemical Engineering

Computational study of crystal breakage with the Cell Average Technique

Master Thesis

Palatos Alexandros

Supervisor
Assistant Professor: Michalis Kavousanakis

Athens, 2022

Abstract

This study concerns the implementation of a computational method simulating ultrasound crystallization breakage. Even though ultrasound has been investigated experimentally, a systematic study of the underlying mechanisms is not yet available. To this end, modeling approaches need to be applied and in particular population balance models that can describe the interplay of various mechanisms. Here, a population balance model (PBM) has been developed to simulate ultrasound crystal breakage process. In this work, the main focus is to investigate crystal breakage with ultrasounds. PBM is a complex class of equations and requires the implementation of numerical techniques. Here, we apply the cell average technique (CAT). We validate CAT by comparing numerical results with simplified PBEs with analytic solutions. Upon validation, we proceed with the comparison of the CAT for pure breakage on crystals with experimental measurements that are provided by the group of professor G. Stefanidis in KU Leuven. We discuss the importance to select an appropriate formulation for the daughter distribution function that describes the breakage mechanism. In order to estimate the necessary breakage kinetic parameters as well as distribution parameters that may be needed, the development of an optimization framework is required. Among the different types of daughter distributions that are modeled, in this work the optimum results are provided using the U-shaped function, which describes the probability distribution of two produced particles after the breakage of the mother crystal. Furthermore, we examine the effect of ultrasound power by fitting for each experiment the corresponding kinetic parameters of the model and derive a power law equation that generalizes our findings. Additionally, we study the effect of ultrasound frequency for three different cases. The majority of the simulations is referred to sodium chlorate, $NaClO_3$, however, we fit the CAT results with the case of L-glutamic acid, LGLu with similar findings.

Εθνικό Μετσόβιο Πολυτεχνείο
Δ.Π.Μ.Σ Υπολογιστική Μηχανική
Τομέας Ρευστών
Σχολή Χημικών Μηχανικών

Υπολογιστική μελέτη του μηχανισμού της διάσπασης κρυστάλλων με τη μέθοδο Cell Average Technique

Μεταπτυχιακή Εργασία

Παλάτος Αλέξανδρος

Επιβλέπων
Επίκουρος Καθηγητής: Μιχάλης Καβουσανάκης

Αθήνα, 2022

Περίληψη

Η παρούσα μελέτη αφορά την εφαρμογή μιας υπολογιστικής μεθόδου για την προσομοίωση διάσπασης κρυστάλλων με υπέρηχους. Παρόλο που η μέθοδος των υπερήχων έχει διερευνηθεί πειραματικά, δεν είναι ακόμη διαθέσιμη μια συστηματική μελέτη των υποκείμενων μηχανισμών. Για το σκοπό αυτό, πρέπει να εφαρμοσθούν προσεγγίσεις μοντελοποίησης και συγκεκριμένα μοντέλα ισοζυγίων πληθυσμών που μπορούν να περιγράψουν την αλληλεπίδραση διαφόρων μηχανισμών. Ως εκ τούτου, έχει αναπτυχθεί ένα μοντέλο ισοζυγίου πληθυσμού (PBM) το οποίο είναι ικανό να προσομοιώνει τη διαδικασία θραύσης κρυστάλλων με υπερήχους. Σε αυτήν την εργασία, το μοντέλο εστιάζει στη διερεύνηση της θραύσης των κρυστάλλων. Το μοντέλο ισοζύγου πλυθησμού είναι μια σύνθετη κατηγορία εξισώσεων και απαιτεί την εφαρμογή αριθμητικών τεχνικών. Σε αυτή τη μελέτη, εφαρμόζεται η μέθοδος διακριτοποίησης cell average technique (CAT). Η ακρίβεια της μεθόδου CAT επιβεβαιώνεται συγκρίνοντας τα αριθμητικά αποτελέσματα με απλοποιημένα μοντέλα ισοζύγιων πλυθησμών, με αναλυτικές λύσεις. Εν συνεχεία, συγκρίνεται η CAT με πειραματικές μετρήσεις, που παρέχονται από την ερευνητική ομάδα του καθηγητή Γ. Στεφανίδη στο KU Leuven, για καθαρή θραύση σε κρυστάλλους. Αναλύεται η σημασία της επιλογής της κατάλληλης εξίσωσης για τη συνάρτηση κατανομής των σωματιδίων που περιγράφει τον μηχανισμό θραύσης. Προκειμένου να εκτιμηθούν οι απαραίτητες κινητικές παράμετροι θραύσης καθώς και οι παράμετροι κατανομής που μπορεί να χρειαστούν, απαιτείται η ανάπτυξη ενός μοντέλου βελτιστοποίησης. Μεταξύ των διαφορετικών τύπων θυγατρικών κατανομών που μοντελοποιούνται, σε αυτήν την εργασία, τα βέλτιστα αποτελέσματα παρέχονται χρησιμοποιώντας τη συνάρτηση σχήματος U, η οποία περιγράφει την κατανομή πιθανότητας δύο παραγόμενων σωματιδίων μετά τη θραύση του μητρικού κρυστάλλου. Επιπλέον, εξετάζεται η επίδραση της ισχύος υπερήχων προσαρμόζοντας για κάθε πείραμα τις αντίστοιχες κινητικές παραμέτρους του μοντέλου και εξάγεται μια εξίσωση νόμου ισχύος που γενικεύει τα αποτελέσματα της μεθόδου. Επιπλέον, μελετάται η επίδραση της συχνότητας των υπερήχων για τρεις διαφορετικές περιπτώσεις. Η πλειονότητα των προσομοιώσεων αναφέρεται στο χλωρικό νάτριο, $NaClO_3$, ωστόσο συγκρίνεται η μέθοδος CAT με μια περίπτωση L-γλουταμινικού οξέος, LGLu, οδηγώντας σε παρόμοια αποτελέσματα.

Contents

1 Introduction

In general, crystallization is an important process for the chemical industry. It is frequently utilized as a purification method. The ability to control the crystal size is of major importance for pharmaceuticals. The requirements are for products of as uniform as possible crystals.

Crystallization is a process during which different sub-processes undergo including nucleation, growth, breakage and agglomeration. All these sub-processes individually, as well as their interplay, control basic properties of the crystals as polymorphic form, size and chirality. In this study, the breakage mechanism is investigated. Generally, the crystal breakage can be achieved by applying stress on the particles. Actually, this pressure is applied either between particles or solid surfaces and particles depending on the specifics of each case. Another breakage method is ultrasound crystal breakage which is investigated in this study. The major advantage of ultrasound compared to the surface stress applying methods is that smaller crystal sizes can be achieved. Therefore, the use of ultrasound in the crystallization process has resulted in better process properties. Although various attempts to examine the sono-crystallization kinetics have been undertaken in the past, only nucleation and crystal growth have been considered [13, 14, 26, 33]. Thus, the main aim of this work is to examine the mechanism of breakage on crystallization procedures.

Many studies relative literature are experimental. Viedma ripening, [63], [64] is a corresponding four stages process that uses crystal breakage to convert a mixture of enantiomers in an enantiopure end product. On the other hand, there is a lack in the studies that relate the kinetics and mechanism of ultrasound facilitated breakage. Consequently, there is a need for computational techniques. The computations are necessary in order to better understand the underlying mechanisms, and of course being able to provide (as accurate as possible) quantitative predictions. This very first step needs experiments for validation. The next step is to use the computational findings and optimize the process, by appropriately modifying various control variables in the procedure. And of course, for upscaling (i.e. application at the industrial level), a computational model is also required. There are various computational methods developed to study crystallization processes. In this work, crystal breakage is simulated using population balance equations (PBEs).

The foundation of population balance equations (PBEs) for particulate processes was laid by Hulburt et al. [17] and developed more specifically from Ramkrishna [46]. The population balance equations (PBEs) are complex partial-integro-differential equations that can be solved analytically only for specific cases. In the case of crystal breakage, the population balance model (PBM) demands the definition and resolution of two kinetic parametric equations, the distribution of daughter particles and the breakage rate. These equations can be used to model and describe processes that involve particle elements. The population balance can be regarded as a balance based on a certain variable such as number or volume. The population balances theory is founded on the idea that the population can be characterized by a continuous function.

There is a variety of computational approaches to deal with PBE in order to extract crystallization kinetics or simulate the evolution of crystal size distribution (CSD) of the crystallization process. In this study, the cell average technique (CAT) for pure crystal breakage will be analyzed. The CAT method was developed by Kumar et al. [23] and has been used extensively in the literature. In most cases, it is difficult to compute an analytic solution for PBE when taking into account the breakage equation. Consequently, analytical solutions of PBE are available only for specific cases. There are a few examples where the computational method can be compared to an analytical solution as Kumar et al. [23] presents. Furthermore, Falola et. al [10] presents some simplified cases where analytical solutions can be included. Consequently, the calculation of the aforementioned breakage equations and the breakage PBE is the main aim of this study. The modeling of a crystal breakage system demands the definition of the breakage kinetic parameters and distribution parameters when needed. Thus, the simulation can be implemented through a necessary, appropriate optimization model, as there are information and measurements for a variety of experimental cases.

2 Literature Review

2.1 Crystallization

Crystallization is the physical transformation of a liquid, solution, or gas into a crystal. Crystal is solid with an ordered internal arrangement of molecules, ions, or atoms. This results in a crystal lattice that extends in all directions. On a macroscopic scale, the crystals are usually identifiable by their geometrical shape, consisting of faces with specific, characteristic orientations. The basic crystal geometries are depicted in Figure 2.1.

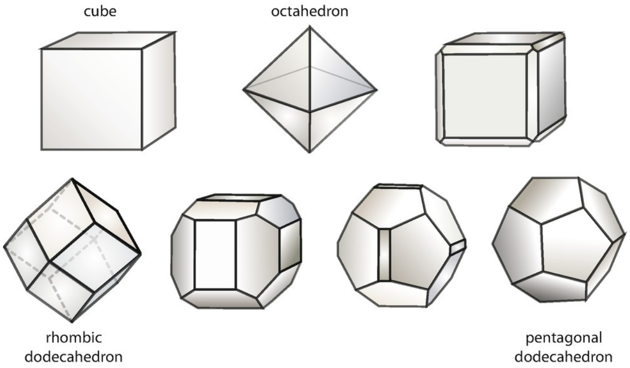

Figure 2.1: Basic shapes of crystals [16].

Many substances studied in research or found in technological and commercial fields are crystalline. In food technology and nutrition i.e., crystalline substances include sugars, sugar alcohols, salts, fats, fatty acids, artificial sweeteners, etc. can be found [5].

The crystallization process can isolate chemical substances in the solid form for long-term storage and downstream processing. The process can be performed under different conditions resulting in various properties on the produced particles. Crystallization has been developed based on thermodynamics, kinetics, fluid dynamics, crystal structures, and inter-facial sciences. Crystallization usually is implemented through precipitating from solution or melt, but can even directly be deposited from a gas.

Crystallization only occurs when supersaturation is created that acts as the driving force for crystallization. From a thermodynamic perspective this driving force is reflected by the difference in chemical potential of the solute in the liquid, μ_L and in the solid phase, μ_S, at temperature T. The aforementioned force represents the supersaturation [21]

$$\Delta\mu = \mu_L(T) - \mu_S(T). \tag{2.1}$$

Cooling crystallization from the melt or the solution

$$\Delta\mu = \frac{\Delta H_{eq}}{T^*}\Delta T, \tag{2.2}$$

where ΔH_{eq} and ΔT denote the enthalpy and temperature differences, respectively. The *eq* index is used to denote the equilibrium phase. For practical reasons the supersaturation in cooling can be defined as

$$\Delta T = T - T^*. \tag{2.3}$$

In the case of melt pressure crystallization

$$\Delta\mu = \Delta V_{molar}\Delta P = \frac{\Delta\rho}{\rho_{melt}\rho_{solid}}\Delta P, \tag{2.4}$$

where ΔV_{molar} denotes the molar volume difference, ΔP and $\Delta\rho$ denote the differences of pressure and density, respectively; ρ_i is the density of each material. For the case of evaporative crystallization (2.1) can be transformed

$$\Delta\mu = RTln\left(\frac{a}{a_{eq}}\right), \tag{2.5}$$

where with a is described the energy per amount of material and R is the gas constant. Supersaturation is a prerequisite factor for crystallization. The formation of a solid is impossible under the solubility threshold. Solubility depends on multiple factors such as temperature, concentration, polarity and ionic strength. Phase diagrams as in Figure 2.2 are commonly used. The figure illustrates three basic stability areas. The stable region or unsaturated region is beneath the solubility threshold. In this region any crystal will dissolve. At the boundary between stable and metastable just when the solution turns from under saturated to supersaturated, the chance for nucleation is small. But the chance increases until the labile zone is reached. In the labile zone, the solution will nucleate spontaneously.

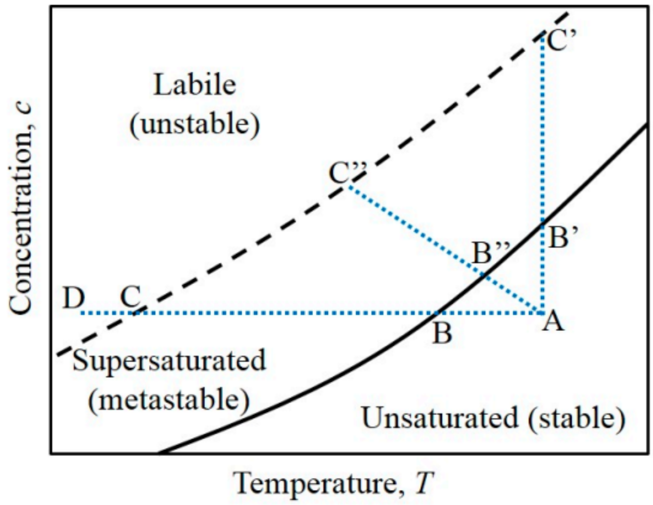

Figure 2.2: Phases of Crystallization [41].

2.2 Mechanisms of Crystallization

The product consists of internal and external states. Composition characteristics constitute the internal states of a crystalline product. The external state of a crystal consists of its geometric position and of the external velocity of the crystal, which gives the change in the external state. The external velocity is a function of both the hydrodynamics of the solid-liquid phase system and the internal states of the crystal.

This section focuses on the main crystallization fundamentals or mechanisms that can change the internal states of a crystalline product. The four basic mechanisms are nucleation, growth, dissolution, agglomeration and attrition or breakage. The internal states determine largely the rates of the events of the aforementioned mechanisms. More precisely, the mechanisms are related with rate coefficients and driving forces, which are defined by slurry states or local process conditions such as supersaturation, energy dissipation, solids concentration, pressure and temperature, as well as internal crystal states, such as size, strain and shape.

2.2.1 Nucleation

Nucleation involves the formation of the new crystalline particles and is classified as being primary or secondary according to the mechanism through which it occurs (figure 2.3).

Primary nucleation includes the development of a new solid phase from a clear solvent. This type of nucleation is further divided into homogeneous and heterogeneous nucleation [21]. In heterogeneous nucleation, nucleation starts on foreign substrates of mostly microscopic particles. In case of absence of the these particles, statistical fluctuations of solute entities clustering together can develop a new phase. This case concerns the mechanism of homogeneous nucleation. The driving force for primary nucleation is the supersaturation of the crystallization system, which is defined as the difference in the chemical potential of the substance in the liquid and the solid phase Eq. (2.1). The rate coefficient or resistance for primary nucleation is a function of the cluster-liquid inter-facial tension and diffusion coefficient. The internal states at the time of nuclei formation such as size, lattice structure and purity, are also related to the supersaturation.

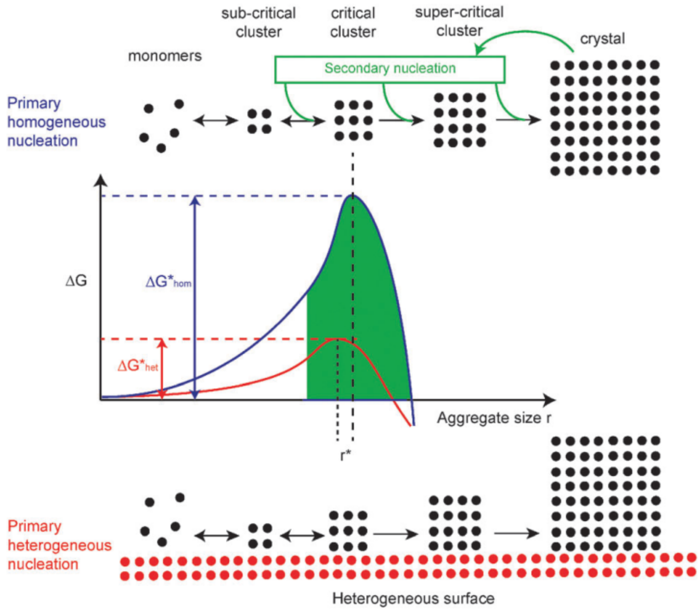

Figure 2.3: Nucleation stages and mechanisms [53].

Secondary nucleation refers to the birth of new crystals at the interface of parent crystals. The mechanism of secondary nucleation does not demand a high level of supersaturation. A supersaturated solution nucleates more readily at a lower level of supersaturation when solute crystals are already present or added. Secondary nucleation also is affected by the hydrodynamics and the suspension density, while the dominant source of secondary nucleation in batch crystallization is attrition.

2.2.2 Crystal Growth

Crystal growth is a major mechanism of a crystallization process, and consists of the addition of new atoms, ions, or polymer strings into the characteristic arrangement of the crystalline lattice [37]. Growth is a mechanism responsible for increasing crystal size, thus essentially determining crystal morphology. The surface structure and the purity of the crystal depend on crystal face growth rates together with the growth mechanism. The growth rates of particular crystal faces usually are not equal, but an overall linear growth rate is often used. Crystal growth is a process consisting of mass transfer, surface integration and heat transfer. Mass transfer and surface integration occur sequentially and in parallel with heat transfer. Mass transfer involves the diffusion of growth units to the crystal surface. Surface integration consists of surface diffusion, orientation and the actual incorporation into the lattice.

2.2.3 Agglomeration

Agglomeration is a particle formation process in which at least two primary particles are combined to form a new one. Agglomerates can be formed by various mechanisms, as for example due to electrostatic forces between nano-particles, the formation of bridges between particles, or by thermal effects, for instance, sintering or glass transition. The formed mass is defined as aggregate in the case of existence of interparticle forces only, such as Van der Waals (attractive), electrostatic (repulsive) and steric forces [45].

The agglomeration mechanism can be divided into primary and secondary. In the latter, the agglomerates are developed by the malformation of crystals. This leads to typical formations such as polycrystals and dendrites. Secondary agglomeration arises in suspended particle systems due to particle collisions. Secondary agglomeration is a phenomenon that takes place in a limited size range from submicron to micron and is negligible beyond 50 mm. The are three main collision mechanisms that lead to particle agglomeration, perikinetic, orthokinetic and inertia. The driving force for agglomeration is supersaturation [40]. Without supersaturation, aggregates can be formed but agglomerates cannot. The rate coefficient or kernel for agglomeration is a function of the number of particles, the size of particles involved, and in the case of orthokinetic agglomeration the fluid shear or energy dissipation.

The properties of the formed agglomerates, e.g. size, shape and porosity, significantly affect certain end-use properties, e.g. dissolubility, processability and storability [51]. Therefore agglomerates are undesirable in many applications, e.g. pharmaceutical manufacturing, food processing and fertilizer production.

2.2.4 Attrition or Crystal Breakage

Attrition is a process that involves either particle-particle or particle-solution interactions. This results in the erosion of the particles known as attrition of particles to produce smaller particles. Disruption kinetics can be modelled for attrition based on a disruption rate [59], [67]. The disruption process is a function of the degree of supersaturation in the crystallizer and hence high supersaturation levels produce high growth rates and therefore stronger agglomerated particles, which reduces the chance of breakage. Increasing the input implies an increase in the disruption rate. Attrition of a particle can lead to the formation of two similar or equal-sized particles (particle splitting), leading to a uniform breakage function, two particles of different size (attrition) leading to a parabolic breakage function, or a number of particles leading to a multiple breakage function. The corresponding particle distributions will be analyzed in the

"Crystal Breakage Kinetics" chapter.

2.3 Viedma Ripening

Viedma ripening or attrition-enhanced deracemization is an isothermal re-crystallization process that allows the complete conversion of a racemic suspension of conglomerate crystals to an enantiopure solid phase by contact with an attrition source, e.g. stirring in the presence of grinding media [69]. It can be classified in the wider area of spontaneous symmetry-breaking phenomena observed in chemistry and physics. It was discovered in 2005 by geologist Cristobal Viedma, who used glass beads and a magnetic stirrer to enable particle breakage of a racemic mixture of enantiomorphous sodium chlorate $NaClO_3$ crystals in contact with their saturated solution in water [64]. Modifications in the initial structure of the experiment allow the modelling various substances such as amino acids [43], [66] and pharmaceuticals [54], [61]. Therefore, Viedma ripening is a new technique to separate enantiomers of chiral molecules in the pharmaceutical and fine chemical industries (chiral resolution). Figure 2.4 presents the procedure of Viedma ripening.

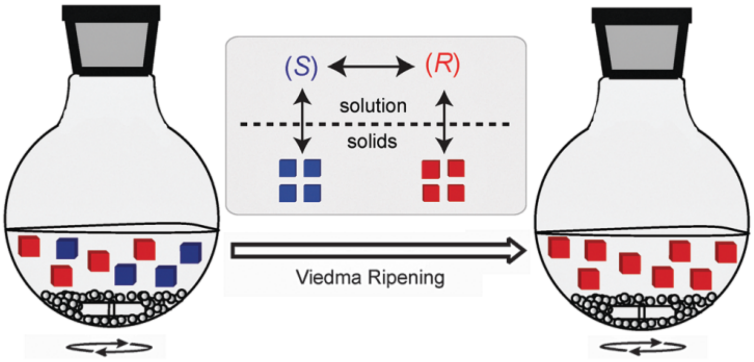

Figure 2.4: Stirring of a racemic mixture of conglomerate crystals in the presence of glass beads (Viedma ripening) [53].

The four stages of the process can be described as follows.

- **Racemization in solution**

  In order to convert all enantiomers in the solid phase to one form, the molecule must continuously racemize in solution. Furthermore, the probability of chiral clusters of the (S)-enantiomer to encounter a crystal of the same handedness is lower and as a consequence, it is harder to dissolve. Therefore, the solution is enhanced with the opposite enantiomer to the one that is enriched in the solid phase. Eventually, the enantiomer in solution undergoes racemization leading to its increase compared to the enantiomer in the solid phase.

- **Ostwald ripening**

  Ostwald ripening, first described by Wilhelm Ostwald in 1896 [38], is the continued dissolution and growth of crystals to reach a thermodynamically stable state wherein the surface area to volume ratio of the solid system is minimized.

- **Aggregation**

  The crystals during the whole process consecutively break into clusters. The reincorporation of these clusters into larger crystallites occurs more often for the enantiomer which is in overabundance in the solid phase. Aggregation combined with attrition have as a result the autocatalytic amplification effect typical for Viedma ripening. Experimental proof for enantioselective incorporation of chiral clusters remains to be found, although some indirect evidence relating to $NaClO_3$, the archetypical compound for Viedma ripening, has been reported.

- **Attrition**

  While enantiopure clusters and molecules of R and S incorporate enantioselectively in the bulk crystals R and S, respectively, the bulk crystals are ground, producing chiral fragments as well as monomers. The steady attrition also maintains overall small crystal sizes which enhance the Ostwald ripening effect. A higher attrition strength implies shorter deracemization times.

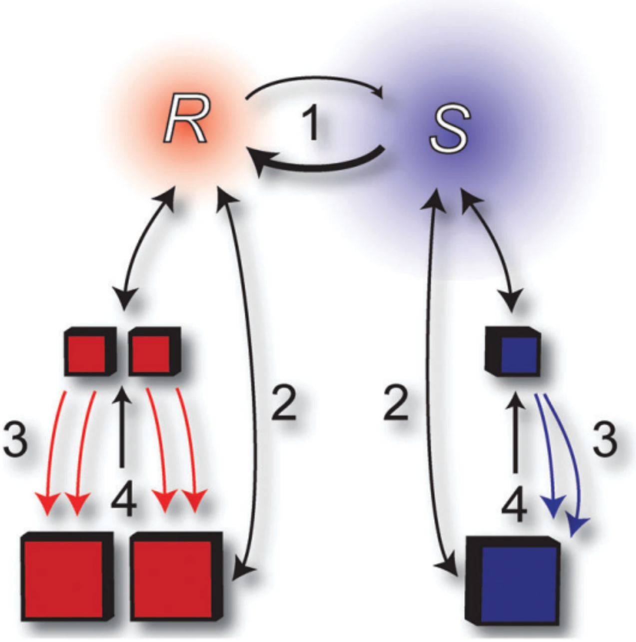

Figure 2.5: Fundamental mechanism of Viedma ripening [53].

2.4 Ultrasound crystal breakage

Ultrasound is an oscillating sound pressure wave over a frequency range of 15 kHz to 10 MHz [57]. When ultrasonic waves of sufficiently high amplitude flow through a liquid, the negative pressure exceeds the liquid's local tensile strength, causing bubbles to form [31]. Bubbles are most commonly formed near pre-existing contaminants that fluctuate and expand during compression and expansion cycles. When the bubbles reach a resonant size, they absorb energy from ultrasound waves efficiently in a single compression-expansion cycle [57,58]. The resonant size varies on the frequency of the irradiated ultrasound and is about 170 µm for a 20 kHz of ultrasound frequency. Due to excellent energy absorption, bubbles develop rapidly at the resonant size within a single cycle of ultrasonic waves. Because bubbles cannot be sustained without absorbing energy, they implode once they reach the resonant size. This procedure is called acoustic cavitation.

Acoustic cavitation has both chemical and physical impacts. In liquid, ultrasonic wavelengths range from 1 mm to 10 cm, which is substantially larger than the molecular size scale. As a consequence, the chemical and physical effects of ultrasound are caused through acoustic cavitation rather than direct interactions between ultrasound and chemical species. [4, 31, 56]. Hot spots are formed when bubbles break down, resulting in high local temperatures (5000 K), pressures (1000 atm) and a rapid heating and cooling rate ($>10^{10}$ K·s $^{-1}$). In heterogeneous systems (solid-liquid systems), ultrasound has a wider range of physical effects than in homogeneous systems. When a bubble collides with a much larger surface or particle, it no longer collapses spherically, and a high-velocity liquid stream with a velocity greater than 100 m/s is created (i.e., a microjet) [3, 28]. The liquid flows toward the solid material's surface, deforming it or altering its chemical composition. Furthermore, high-velocity collisions between micron-sized solid particles are caused by shockwaves created by acoustic cavitation (i.e., interparticle collisions). Shockwaves can also contact directly with particles, causing them to break (i.e., sonofragmentation).

Richards and Loomis initially described sonocrystallization (crystallization caused by ultrasonic) in 1927 [49]. The authors of that work focused on the impacts of ultrasonic crystallization, amid a slew of other physical and chemical factors. Sonocrystallization was actively explored in the former Soviet Union from the 1950s to the 1970s [2, 19, 44, 62]. Due to the development of ultrasonic equipment, industrial use increased in the 1980s, and it is now widely used in the pharmaceutical and fine chemicals industries to generate crystals [6, 7, 50]. Despite extensive research, a basic understanding of sonocrystallization mechanism is still lacking.

2.5 Crystallization process applications

There is a variety of crystallization applications both at the laboratory and industrial levels. As far as the former is concerned crystallization can be used to investigate the structure and isolation of proteins. Until now, the analysis of proteins is carried out mainly by X-ray crystallography, which relies on the presence of crystals of appropriate size and quality [39]. These criteria are met through crystallization, which can be done in a variety of ways.

On an industrial scale, crystallization has applications in the production of bulk chemicals such as sucrose and many minerals (chlorides, sulfates, chlorides) [48], in the production of fertilizers such as ammonium nitrate, potassium chloride and urea, cosmetics, medicines, food and products in electronics [32]. The most well-known bulk chemical produced by crystallization is table salt, as worldwide its production exceeds 10^8 tons each year. The salt is separated from the water by evaporation. The solution reaches its boiling point at a given pressure and temperature, at which point the water evaporates and the salt concentration in the remaining solution rises. As a result, nucleation and crystal formation commence [21].

In the pharmaceutical industry, crystallization is used in the separation of enantiomers, the manufacturing of active pharmaceutical ingredients (APIs), and the administration of pharmaceuticals through methods such as controlled inhalation and intravenous injection. More specifically, in drugs administered by the lung, the size distribution of the crystals must be characterized by modest dispersion (narrow distribution), hence the crystallization procedure is crucial. Larger crystal sizes than foresight will not reach the appropriate areas (loop and alveoli), while smaller can pass through lung tissue [29]. In general, smaller particles have a higher surface to volume ratio which is beneficial for the solubility and dissolution rate. Therefore, these qualities improve the effects of the medicine.

In the food industry, control of crystallization is crucial for the quality of products and their shelf life. In some foods, the presence of crystals is desirable while in others it should be avoided. The presence of cocoa crystals in chocolate, for example, is a key component of its flavor, but lactose crystals in ice cream provide an unpleasant texture that renders it undesirable. They also become unsuitable for other foods like cheddar cheese, some candies and hard candies with the appearance of crystals during storage [15].

In the field of electronics, the crystallization of polymers is used for the production of thin films which are necessary for applications such as the production of transistors and solar cells. Thin perovskite films employed as photovoltaics, for instance, are sensitive to their shape. The morphology controlled by the crystallization process has a great effect on the performance of the solar cell as well as poor morphology (rough outer surface) results in electrical short circuits. For this reason, special attention is paid to the nucleation and development of their crystals. [34]. The yield of transistors is affected by the crystallization parameters, just as it is in solar cells. In this case, it is the size of the crystals in the semiconductor that needs to be modified [30].

2.6 Experimental and Computational approaches of Crystallization

Cristobal Viedma used glass beads and a magnetic stirrer to enable particle breakage of a racemic mixture of enantiomorphous sodium chlorate $NaClO_3$ crystals in contact with their saturated solution in water [64]. The study comprised the first crystallization experiment to induce homochirality and chiral purity from a system in which both enantiomers were present. Previously, chiral purity could only be attained by seeding the solution.

In 2008 Noorduin et al. recreated the experiment that Viedma had performed. However, they employed amino acid derivatives, which have chirality in the dissolved phase, extending the ripening process of Viedma to other molecules. They also managed to increase the volume of the original experiment, indicating that it may be used at the industrial level.

Rene Steendam's work [55] on Viedma ripening looked into the impact of chiral impurities. Even though spontaneous symmetry breaking and chiral amplification via Viedma ripening should result in complete deracemization of a racemic conglomerate into either of the enantiomers with equal probability, this is not the case in practice. Viedma ripening is influenced by chiral impurities, and one enantiomer is favored over the other. Increasing the attrition intensity during Viedma ripening was the solution. As a result, contaminants do not affect the likelihood of either enantiomer forming. According to the findings, higher attrition resulted in smaller crystals with lower impurity surface density, however, this is insufficient to determine the chiral outcome.

Xiouras et al. [70] examined two ways of attrition-enhanced deracemization for $NaClO_3$. In this study, Viedma's original experiment with glass bead-enhanced grinding was compared against ultrasound-enhanced grinding, while for large-scale or continuous-flow processes, this is a more practical option. In comparison with glass bead-enhanced grinding, the results demonstrated that ultrasound grinding produced smaller crystals with a narrower crystal size distribution. Furthermore, ultrasonography boosts the pace of initial deracemization. The ultrasound, however, did not result in a fully enantiopure end product. To solve this, they utilized seeding or a hybrid procedure that blended the two methods. Both options resulted in enantiopurity in the end. Additionally, Xiouras et al. [68] through three sections of experiments describe the particle breakage kinetics and mechanism from the parallel phenomena (growth-dissolution, agglomeration).

Crystallization is an important process for various industrial and research fields. However, the experimental procedures are difficult to be applied in the industry, since the mechanisms are still investigated. There are obstacles in adapting the experiments to industrial scale and there is a need for up-scaling and process optimization. Therefore, the implementation of computational methods for the simulation of crystallization processes is of great importance. Uwaha presented one of the first models for Viedma ripening [60]. To explain the progression to an enantiopure product, he employed a reaction-type model, taking into account only the total number of crystals in each configuration, monomers in solution, and chiral clusters. Although the model was able to reproduce some experimental results, it was unable to explain size-dependent effects.

Population balance model simulating the Viedma ripening was utilized in the work of Iggland et al. [18]. Details for population balance model theory will be provided in the "Mathematical Model" chapter. Stochastic algorithms like Monte Carlo have been developed in order to solve population balance equations [35], [18]. Computational fluid dynamics (CFD) methods and more precisely the finite volume discretization has been developed by Wang and Wang [65] and Kumar et al. [22]. Additionally, Grof et al. [12] used a discrete element method (DEM) to solve a population balance model (PBM). Moreover, the method of moments for solving the population balances associated with simultaneous coagulation and breakage is presented in the work of Diemer and Olson [8].

The fixed pivot technique (FPT) was introduced by Kumar [25]. Kostoglou [20] compared the FPT with the cell average technique (CAT). The latter was developed by Kumar et al. [24] and has been used extensively in the literature. In this study, the cell average technique for the mechanisms of crystal breakage, agglomeration and the combination of the aforementioned procedures will be analyzed.

3 Mathematical Model

3.1 Population Balance Equations (PBEs)

Population balance equations have been developed to describe particle systems. The processes that can be modeled using PBEs are characterized by the coexistence of a continuous and a dispersed phase consisting of particles. In this study the dispersed phase involves crystals. There are properties of the particles like size, porosity, composition, etc. that are not constant and can be described with distributions. This work is about the modeling of crystals that are created through breakage and the variation of their size distribution.

The particle state can be described by a partitioned vector $[x_1, x_2, ..., x_m]$ where x_i represents the vector of n components in the i_{th} compartment. A distinction is made between external coordinates $r = (r_l, r_2, r_3)$, which may be used to represent the position vector of the particle (as determined by that of its centroid), and internal coordinates $x = (x_l, x_2, ..., x_d)$ denoting d different quantities associated with the particle. The particle state vector (x, r) accounts for both internal and external coordinates. The continuous phase is defined by a continuous phase vector $Y(r,t) = [Y_1(r,t), Y_2(r,t), ..., Y_c(r,t)]$, as a function of external coordinates r and time t.

An average number density function can be defined in the particle state space

$$E\left[(n(x,r,t))\right] = f_1(x,r,t), \qquad x \in \Omega_x, \qquad r \in \Omega_r. \tag{3.1}$$

The left-hand side of the Eq.(3.1) denotes the expectation or the average of the actual number density $n(x,r,t)$ while the right-hand side displays the average number density $f_1(x,r,t)$. The Ω_x and Ω_r terms represent the domains of internal and external coordinates, respectively.

The average total number of crystals in the entire system can be defined as

$$N_{total} = \int_{\Omega_x} \mathrm{d}V_x \int_{\Omega_r} \mathrm{d}V_r f_1(x,r,t). \tag{3.2}$$

The local (average) number density in physical space, i.e., the (average) total number of particles per unit volume of physical space, denoted $N(r,t)$, is given by

$$N(r,t) = \int_{\Omega_x} \mathrm{d}V_x f_1(x,r,t). \tag{3.3}$$

In the same way, other densities such as volume or mass density can also be defined for the particle population.

Generally, the population balance equation describes the equilibrium as

$$Accumulation = Inflow - Outflow. \tag{3.4}$$

Where the left-hand side of Eq. (3.4) stands for the rate of change of crystal population. The inflow term is about the movement and the creation of new crystals inside the defined space, while the outflow term describes the corresponding crystal movements when their size becomes bigger than the examined space.

Assuming a population of crystals of different sizes distributed according to their size x which varies between 0 and ∞. The particles are uniformly distributed in space and there is no dependence on the external coordinates. The growth rate of particles can be denoted with $\dot{X}(x,t)$ and the number density function is denoted as $f_1(x,t)$. The rate of change in the interval $[x, x+dx]$ described as

$$\dot{X}(x,t)f_1(x,t) - \dot{X}(x+dx,t)f_1(x+dx,t), \tag{3.5}$$

where the terms in Eq. (3.5) represent particle fluxes in x and $x+dx$, respectively. Considering that particles can move between intervals only due to growth the number balance can be formulated as

$$\frac{d}{dt}\int_a^b f_1(x,t)\mathrm{d}x = \dot{X}(x,t)f_1(x,t) - \dot{X}(x+dx,t)f_1(x+dx,t). \tag{3.6}$$

The Eq. (3.6) can be rewritten as

$$\int_a^b \left[\frac{\partial f_1(x,t)}{\partial t} + \frac{\partial}{\partial x}\left(\dot{X}(x,t)f_1(x,t)\right)\right]\mathrm{d}x = 0. \tag{3.7}$$

Therefore, the population balance equation can be written as

$$\frac{\partial f_1(x,t)}{\partial t} + \frac{\partial}{\partial x}\left(\dot{X}(x,t)f_1(x,t)\right) = 0. \tag{3.8}$$

The necessary boundary and initial conditions of the PBE Eq. (3.8) have to been defined. The assumption of an initial number of particles n_0 leads to the initial condition $f_1(x,0) = 0$. For the boundary condition the nucleation rate can be $\dot{n}_0$ particles per unit and the assumption that newly born particles have zero mass is made. Thus

$$\dot{X}(0,t)f_1(0,t) = \dot{n}_0 \tag{3.9}$$

If Eq. (3.8) is integrated over all particle sizes

$$\frac{d}{dt}\int_0^\infty f_1(x,t)\mathrm{d}x = \dot{X}(0,t)f_1(0,t) - \dot{X}(\infty,t)f_1(\infty,t) = \dot{n}_0, \tag{3.10}$$

which leads to the consumption that

$$\dot{X}(\infty,t)f_1(\infty,t) = 0. \tag{3.11}$$

Equation (3.9) is the required boundary condition while (3.11) in the literature is referred as regularity boundary condition.

In the above analysis, were not been envisaged the birth and death of particles in the interval $[x, x+dx]$. In the case of breakage and aggregation, for example, the net rate of generation of particles can be denoted with $h(x,t)$ and depends on each mechanism. Thus, the equation (3.7) will be replaced from

$$\int_a^b \left[\frac{\partial f_1(x,t)}{\partial t} + \frac{\partial}{\partial x}\left(\dot{X}(x,t)f_1(x,t)\right) - h(x,t)\right]\mathrm{d}x = 0, \tag{3.12}$$

and the PBE will take the form

$$\frac{\partial f_1(x,t)}{\partial t} + \frac{\partial}{\partial x}\left(\dot{X}(x,t)f_1(x,t)\right) = h(x,t). \tag{3.13}$$

Consider the continuous phase to be described by a scalar quantity Y, which is assumed to be uniform in space. In a well-mixed crystallizer, Y may represent the supersaturation at the surface of the crystals. In this case the nucleation rate depends on Y, i.e., $\dot{n}_0 = \dot{n}_0(Y)$. Moreover, the growth rate may be depended Y as $\dot{X} = \dot{X}(x,Y,t)$.

So, the proper definition for Eq. (3.13) is

$$\frac{\partial f_1(x,t)}{\partial t} + \frac{\partial}{\partial x}\left(\dot{X}(x,Y,t)f_1(x,t)\right) = h(x,Y,t). \tag{3.14}$$

The initial condition remains the same as before while the boundary condition recognizes the dependence of the nucleation and growth rates on Y. Thus

$$\dot{X}(0,Y,t)f_1(0,t) = \dot{n}_0(Y). \tag{3.15}$$

To solve the problem, it is necessary to define an initial condition for Y depending on the mechanism that is modeled.

The reason for neglecting breakage and agglomeration during sonocrystallization lies in the complexity of the mathematical modeling of crystallization in general. The modeling of the crystallization process is performed using PBE. A population balance is a means of keeping track of numbers of entities whose presence or occurrence may dictate the behavior of the system under study. PBE coupled with mass and energy balance equations describes the crystallization process mathematically. Additionally, it is assumed that the particles are cubic, and the formulation as well as the solution of the equations implemented in the volume of particles which is denoted as $x = L^3$, where L represents the particle length in μm.

A general one-dimensional PBE for a well mixed system for the four mechanisms of growth, nucleation, breakage and aggregation can be described as

$$\begin{aligned}\frac{\partial n(t,x)}{\partial t} =& \frac{Q_{in}}{\tilde{V}}n_{in}(x) - \frac{Q_{out}}{\tilde{V}}n_{out}(x) - \frac{\partial[G(t,x)n(t,x)]}{\partial x} \\ &+ B_{nuc}(t,x) + B_{break}(t,x) + B_{agg}(t,x) \\ &- D_{break}(t,x) - D_{agg}(t,x).\end{aligned} \tag{3.16}$$

The first two terms on the right-hand side represent the flow into and out of a continuous process. The symbols Q_{in} and Q_{out} denote the inlet and outlet flow rates from the system. The $B_{break}(t,x)$ and $D_{break}(t,x)$ term stand for birth and death of particles in the breakage process, respectively. Along the same lines, the birth and death terms for the aggregation process are defined by the terms $B_{agg}(t,x)$ and $D_{agg}(t,x)$, while $B_{nuc}(t,x)$ and $G(t,x)$ describe the nucleation and growth rates, respectively. The system volume is represented by $\tilde{V}$. The main purpose of this work is the investigation of the pure breakage mechanism.

3.2 The Cell Average Technique (CAT)

The cell average technique (CAT) is a method for solving partial integral equations. This method was developed by Kumar [23] and it is a discretization method. The CAT was chosen because it is the only technique that is consistent with two moments. Equation (3.17) describes the j_{th} moment of a particle size distribution (PSD). The first two moments represent some important characteristics of the distribution. The zeroth ($j = 0$) and first ($j = 1$) moments are proportional to the total number and total mass of particles, respectively [24].

$$\mu_j = \int_0^\infty x^j n(t,x)\mathrm{d}x. \tag{3.17}$$

CAT method is also proven to be more accurate than other methods applied to analytical solutions. In what follows the general concept of the cell average technique will be explained. Afterwards, it will be applied to the particular breakage problem. The goal of the cell average technique is to transform the general continuous population balance equation into a set of discrete ODEs.

The entire size domain is divided into a finite number I of small cells. The lower and upper boundaries of the i_{th} cell are denoted with $x_{i-1/2}$ and $x_{i+1/2}$, respectively. All particles belonging to a cell are identified by a representative size of the cell, also called grid point. This cell size can be chosen at any position between the lower and upper boundaries of the cell. In this work, the center of the cell, the arithmetic mean of the cell boundaries, is defined as the representative size.

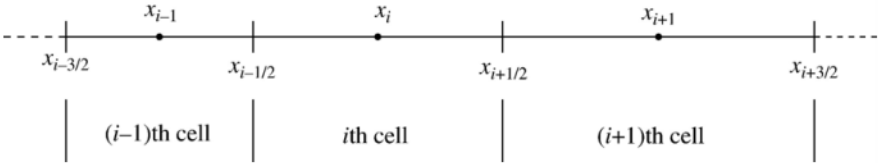

Figure 3.1: CAT 1D domain discretization [24].

The aim is to transform the general continuous population balance equation into a set of I ODEs. The numerical solution of the resulting ODE set can be obtained by well-established numerical techniques (ode solvers). For the i_{th} cell of the discretized domain the ODE has the following form

$$\frac{dN_i}{dt} = B_i^{CA} - D_i^{CA}, \qquad i = 1, 2, ..., I, \tag{3.18}$$

where the CA exponent stands for Cell Average. The particulate events that may change the concentration number of particles include the four basic crystallization mechanisms, breakage, aggregation, growth and nucleation.

The total birth of particles in the i_{th} cell can be calculated as

$$B_i = \sum_{j=1}^{I_i} B_i^j. \tag{3.19}$$

Assuming that the particle births $B_i^1, B_i^2, ..., B_i^I$ take place at positions $y_i^1, y_i^2, \ldots, y_i^I$, respectively due to some particulate processes in the cell i. The average volume of newborn particles $\overline{v}_i$ can be defined as

$$\overline{v}_i = \frac{\sum_{j=1}^{I_i} y_i^j B_i^j}{B_i}. \tag{3.20}$$

Generally the B_i particles are found in the interval $\left[x_{i-1/2}, x_{i+1/2}\right]$. If the average volume $\overline{v}_i$ matches with the representative size x_i then the total birth B_i can be assigned to the node x_i. But this is rarely true, hence the total particle birth B_i has to be reassigned to the neighbouring nodes in order to obtain mass equilibrium. The particles have to be distributed among the neighboring cells in a way that guarantees consistency with the first two moments. Therefore, it is necessary to apply the following transformations for the two first moments

$$a_1(\overline{v}_i, x_i) + a_2(\overline{v}_i, x_{i+1}) = B_i, \tag{3.21}$$

$$x_i a_1(\overline{v}_i, x_i) + x_{i+1} a_2(\overline{v}_i, x_{i+1}) = B_i \overline{v}_i. \tag{3.22}$$

The terms $a_1(\overline{v}_i, x_i)$ and $a_2(\overline{v}_i, x_{i+1})$ stand for the fractions of the birth term B_i to be assigned at x_i and x_{i+1}, respectively. The above equations can be solved for the aforementioned fractions as

$$a_1(\overline{v}_i, x_i) = B_i \frac{\overline{v}_i - x_{i+1}}{x_i - x_{i+1}} \tag{3.23}$$

$$a_2(\overline{v}_i, x_{i+1}) = B_i \frac{\overline{v}_i - x_i}{x_{i+1} - x_i} \tag{3.24}$$

To simplify calculations the lamda function is denoted as

$$\lambda_i^{\pm}(x) = \frac{x - x_i \pm 1}{x_i - x_i \pm 1} \tag{3.25}$$

Thus, the fractions can be expressed in terms of λ as

$$a_1(\overline{v}_i, x_i) = B_i \lambda_i^{+}(\overline{v}_i) \tag{3.26}$$

$$a_2(\overline{v}_i, x_{i+1}) = B_i \lambda_{i+1}^{-}(\overline{v}_i) \tag{3.27}$$

The birth term consists of four possible birth fractions that may add a birth contribution at the node x_i: two from the neighboring cells and two from the i_{th} cell. All possible birth contributions are shown in Figure 3.2.

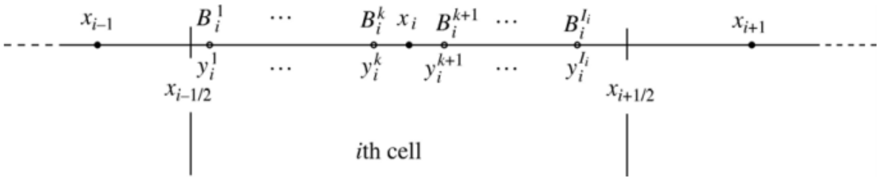

Figure 3.2: Particles in a cell [24].

Collecting all birth contributions, the birth term for the cell average technique is given by

$$\begin{aligned} B_i^{CA} =& B_{i-1}\,\lambda_i^-(\overline{v}_{i-1})H(\overline{v}_{i-1}-x_{i-1}) + B_i\,\lambda_i^-(\overline{v}_i)H(x_i-\overline{v}_i) \\ &+ B_i\,\lambda_i^+(\overline{v}_i)H(\overline{v}_i-x_i) + B_{i+1}\,\lambda_i^+(\overline{v}_{i+1})H(x_{i+1}-\overline{v}_{i+1}) \end{aligned} \tag{3.28}$$

Where the $H(x)$ stands for Heavyside Function:

$$H(x) = \begin{cases} 1\,, & x > 0 \\ 1/2\,, & x = 0 \\ 0\,, & x < 0 \end{cases} \tag{3.29}$$

3.3 CAT Implementation

3.3.1 Pure Breakage

The mechanism studied in this work is the crystal breakage, thus Eq. (3.16) can be simplified as follows:

$$\frac{\partial n(t,x)}{\partial t} = B_{break}(t,x) - D_{break}(t,x). \tag{3.30}$$

The population balance equation for breakage (Eq. (3.30)) simply gives a balance stating that the change in the number of particles is given as the difference between births and deaths of crystals. A crystal that breaks is considered a death contribution and will give rise to new smaller crystals which are the births for cells at smaller x_i. There are three different functions present and they depend on three different variables. These variables are t, x and x' which stand respectively for time, crystal size and crystal size of a mother crystal particle. The term $n(x,t)$ stands for the density distribution and $n(x)dx$ gives the number of crystals with size in the interval $[x-dx, x+dx]$. The functions $b(x,x')$ and $S(x)$ give the particle size distribution (PSD) of the daughter particles for a given mother particle and the specific breakage rate which indicates how often crystals break, respectively. These functions are the two major breakage equations and they are unknown in general. They depend on the system that is modeled and as a consequence the necessity of computational models is significant in order to investigate their exact form. The aforementioned equations are thoroughly analyzed in the "Crystal Breakage Kinetics" chapter.

$$\frac{\partial n(x,t)}{\partial t} = \int_x^\infty b(x,x')S(x')n(t,x')\mathrm{d}x' - S(x)n(t,x). \tag{3.31}$$

On the right-hand side of Eq. (3.31), the first part stands for the birth term, while the second one is the death term, respectively. With the implementation of CAT, the total birth and death rates of particles in the i_{th} cell are calculated by integrating the birth and death rates in the interval $\left[x_{i-1/2}, x_{i+1/2}\right]$ as

$$B_{break,i} = \int_{x_{i-1/2}}^{x_{i+1/2}} \int_x^\infty b(x,x')S(x')n(t,x')\mathrm{d}x'\mathrm{d}x, \tag{3.32}$$

$$D_{break,i} = \int_{x_{i-1/2}}^{x_{i+1/2}} S(x)n(t,x)\mathrm{d}x. \tag{3.33}$$

The total volume flux as a result of breakage into the cell i is needed to calculate the average volume (3.39) and it is given by

$$V_{break,i} = \int_{x_{i-1/2}}^{x_{i+1/2}} \int_{x}^{\infty} xb(x,x')S(x')n(t,x')\mathrm{d}x'\mathrm{d}x. \tag{3.34}$$

The continuous number density function $n(t,x)$ can be approximated in terms of Dirac-delta distribution as

$$n(t,x) \approx \sum_{i=1}^{I} N_i \delta(x - x_i). \tag{3.35}$$

Substituting the Dirac-delta mass representation (3.35) of the continuous number density $n(t,x)$ into the above birth, volume and death rates, the equations are become:

$$B_{break,i} = \sum_{k \geq i} N_k(t) S_k \int_{x_{i-1/2}}^{p_k^i} b(x, x_k)\, dx, \tag{3.36}$$

$$V_{break,i} = \sum_{k \geq i} N_k(t) S_k \int_{x_{i-1/2}}^{p_k^i} b_x(x, x_k)\, dx, \tag{3.37}$$

$$D_{break,i} = S_i\, N_i(t). \tag{3.38}$$

by dividing the total volume birth $V_{break,i}$ by the total number birth $B_{break,i}$, we obtain the volume average $\overline{v}_{break,i}$ in the i_{th} cell as

$$\overline{v}_{break,i} = \frac{V_{break,i}}{B_{break,i}}. \tag{3.39}$$

3.3.2 Breakage and Aggregation

In the case of the combination of breakage and aggregation mechanisms the main PBE (3.16) can be formed as

$$\frac{\partial n(t,x)}{\partial t} = B_{break}(t,x) + B_{agg}(t,x) - D_{break}(t,x) - D_{agg}(t,x). \tag{3.40}$$

In the assumption of combined breakage and aggregation the PBE has the following form

$$\begin{aligned} \frac{\partial n(x,t)}{\partial t} = & \underbrace{\int_{x}^{\infty} b(x,x')S(x')n(t,x')\mathrm{d}x' - S(x)n(t,x)}_{\text{breakage}} + \\ & \underbrace{\frac{1}{2}\int_{0}^{x} \beta(t, x-x', x')n(t, x-x')n(t,x')\mathrm{d}x' - n(t,x)\int_{0}^{\infty} \beta(t,x,x')n(t,x')\mathrm{d}x'}_{\text{aggregation}}. \end{aligned} \tag{3.41}$$

The β term in (3.41) denotes the coagulation kernel and it represents properties of the physical medium. Similarly with pure breakage applying the CAT the birth and death terms for pure aggregation can be denoted in the interval $\left[x_{i-1/2}, x_{i+1/2}\right]$ as

$$B_{agg,i} = \frac{1}{2}\int_{x_{i-1/2}}^{x_{i+1/2}} \int_{0}^{x} \beta(t, x-x', x') n(t, x-x') n(t, x') \mathrm{d}x' \mathrm{d}x, \tag{3.42}$$

$$D_{agg,i} = \int_{x_{i-1/2}}^{x_{i+1/2}} \left[n(t,x) \int_{0}^{\infty} \beta(t, x, x') n(t, x') \mathrm{d}x' \right] \mathrm{d}x. \tag{3.43}$$

Substituting the Dirac-delta mass representation (3.35) of the continuous number density $n(t, x)$ into the above birth and death rates, the equations are formed as

$$B_{agg,i} = \sum_{\substack{j,k \\ x_{i-1/2} \le (x_j + x_k) < x_{i+1/2}}}^{j \ge k} \left(1 - \frac{1}{2}\delta_{j,k}\right) \beta_{j,k} \, N_j \, N_k, \tag{3.44}$$

$$D_{agg,i} = N_i \sum_{k=1}^{I} \beta_{i,k} \, N_k. \tag{3.45}$$

The total volume flux as a result of breakage into the cell i is needed to calculate the average volume (3.47) and it is given by

$$V_{agg,i} = \sum_{\substack{j,k \\ x_{i-1/2} \le (x_j + x_k) < x_{i+1/2}}}^{j \ge k} \left(1 - \frac{1}{2}\delta_{j,k}\right) \beta_{j,k} \, N_j \, N_k \left(x_j + x_k\right). \tag{3.46}$$

The average volume of all newborn particles can be calculated as in the case of pure breakage in the i_{th} cell as

$$\overline{v}_{agg,i} = \frac{V_{agg,i}}{B_{agg,i}}. \tag{3.47}$$

When combining breakage and aggregation, the birth, death and average volume terms can be expressed as

$$B_i = B_{break,i} + B_{agg,i} \tag{3.48}$$

$$D_i = D_{break,i} + D_{agg,i} \tag{3.49}$$

$$\overline{v}_i = \frac{V_{break,i} + V_{agg,i}}{B_{break,i} + B_{agg,i}} \tag{3.50}$$

The total birth term is denoted in Eq. (3.28) as

$$\begin{aligned} B_i^{CA} &= B_{i-1} \, \lambda_i^{-}(\overline{v}_{i-1}) H(\overline{v}_{i-1} - x_{i-1}) \\ &+ B_i \, \lambda_i^{-}(\overline{v}_i) H(x_i - \overline{v}_i) \\ &+ B_i \, \lambda_i^{+}(\overline{v}_i) H(\overline{v}_i - x_i) \\ &+ B_{i+1} \, \lambda_i^{+}(\overline{v}_{i+1}) H(x_{i+1} - \overline{v}_{i+1}) \end{aligned} \tag{3.51}$$

The total death term is defined directly from Eq. (3.49)

$$D_i^{CA} = D_i \tag{3.52}$$

Finally, the requested ODEs system (3.18) can be solved for pure breakage, pure aggregation, or the combination of both the aforementioned mechanisms.

3.4 Crystal Breakage Kinetics

The population balance equation for breakage, Eq. (3.31).

$$\frac{\partial n(x,t)}{\partial t} = \int_x^\infty b(x,x')S(x')n(t,x')\mathrm{d}x' - S(x)n(t,x). \tag{3.53}$$

Where t, x and x' denote time, crystal size and crystal size of a mother crystal particle, respectively. Furthermore, The term $n(x,t)$ denotes the crystal size distribution and gives the number density distribution at different times. The objective is to find this function as a result of the given input. The particle size distribution of the daughter particles function, $b(x,x')$ and the breakage rate, $S(x)$ are investigated in the following paragraphs.

3.4.1 Breakage Rate

The breakage rate usually depends on the problem that is simulated. This calls for a different approach when a function with several parameters is fitted to closely approximate given experimental data. The basic form of the breakage rate is a power law such as the one given in equation (3.54). This form is based on the derivation from Kusters et al. [27] for ultrasound breakage. The parameters S_1 and m are the kinetic parameters and have to be positive constants.

$$S(x) = S_1 x^m \tag{3.54}$$

The selection rate constant S_1 and the exponential constant m are related to the cavitation rate. For any $m > 0$, this expression has the breakage rate approaching zero as the crystal volume x approaches zero. The dynamics of the number density function slow down, i.e., significant changes are observed at the start of the process, but things gradually slow down until appearing to approach a limiting value over the finite time duration of the single experiment. Experimentally, the cavitation rate was observed to be related to the liquid viscosity [47]. Thus, an expression for S_1:

$$S_1 = S_0 P^n. \tag{3.55}$$

In Eq. (3.55) the variable P denotes the ultrasound power in Watt, while the exponential parameter n is related to the liquid viscosity.

The theory about breakage rate for ultrasound breakage can be found in the work of Kusters et al. [27]. It is assumed that the breakage rate of a particle of size x, $s(x)$ is proportional to the number of collapsing cavities per unit time denoted by N_c:

$$S(x) \sim \frac{N_c V_c}{V_{tot}}. \tag{3.56}$$

The variable V_c stands for the volume around an imploding cavity, while V_{tot} represents the total suspension volume. In the ultrasound breakage, agglomerates can break with two different mechanisms. The first one is the results of high pressure in the vicinity of a collapsing cavity. The second one is by induced by liquid jets resulting from the collapse of adjacent cavities. The volume surrounding a cavity denoted as

$$V_c = \frac{4}{3}\pi\left((R_b + R_a)^3 - R_b^3\right). \tag{3.57}$$

Breakage requires the agglomerates have to be close to the cavities. As a result, only agglomerates at the cavities' edges collapse. This is depicted in Figure 3.3.

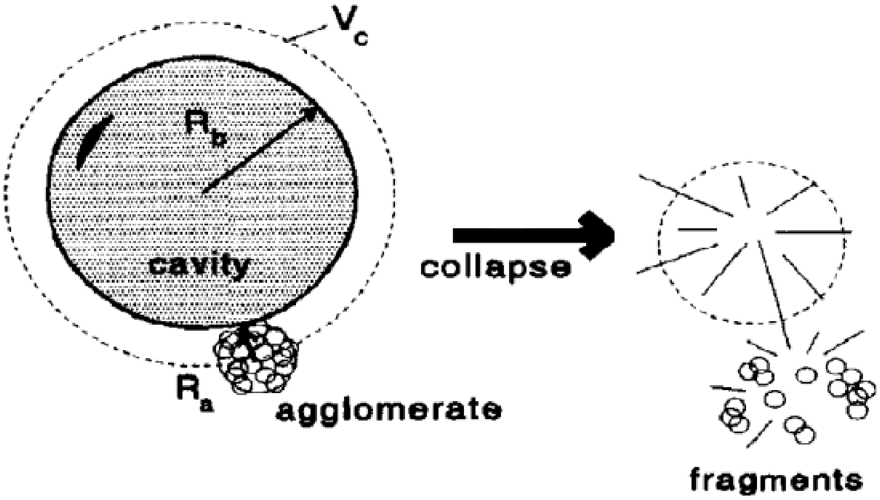

Figure 3.3: Agglomerate rupture in close proximity to a collapsing cavity [27].

For non spherically shaped agglomerates, R_a and φ denote the equivalent spherical radius and solids volume fraction, respectively, of the agglomerate. Usually, the agglomerate radius R_a is negligible ahead cavity radius R_b. Hence, V_c, can be approximated by

$$V_c = 4\pi R_b^2 R_a. \tag{3.58}$$

In the case of spherical shaped agglomerates of radius R_a, with solids volume fraction φ, the relationship between the agglomerate radius R_b, and solids volume v is

$$v = \frac{4}{3}\pi R_a^3 \varphi. \tag{3.59}$$

Taking into account the previous analysis, a relation between the breakage rate can be expressed as

$$S(x) \sim \frac{N_c R_b^2 v^{1/3}}{V_{tot}} \tag{3.60}$$

The energy lost E upon collapsing cavities can be defined as [9]:

$$E = \frac{4}{3}\pi R_b^3 \Delta P. \tag{3.61}$$

Where ΔP stands for the pressure difference between the cavity wall, during the time of collapsing. Considering that only a fraction κ of the ultrasonic power ε is used to create cavities a relation between the number of collapsing cavities can be denoted as

$$N_c \sim \frac{\kappa\varepsilon}{\frac{4}{3}\pi R_b^3 P_h}. \tag{3.62}$$

A relationship between maximum radius of cavities and ultrasound power can be expressed as [52]

$$R_B \sim \varepsilon^{1/2}. \tag{3.63}$$

Substituting these in the original expression for the breakage rate ultimately gives the final relation

$$S(x) \sim \frac{\kappa\varepsilon^{1/2} v^{1/3}}{V_{tot}}. \tag{3.64}$$

In this thesis, the generalized power law breakage rate, Eq. (3.54) is used, because the crystals are considered to be cubic shaped, and the main purpose is to investigate the influence of the kinetic parameters S_1 and m.

3.4.2 Daughter Distribution

The daughter distribution formulates the particle size distribution of the newborn particles for a given mother particle. A mother particle is an original crystal that breaks and as a result, produces new smaller particles. A daughter distribution gives insight into the breaking mechanism. The selection of the daughter distribution is important for the crystal breakage simulation and it is system- specific. A main purpose of this work is to formulate an appropriate distribution for ultrasound breakage. Daughter distribution can describe the average number of particles per breakage as

$$N_p = \int_0^{x'} b(x, x')\,\mathrm{d}x'. \tag{3.65}$$

One of the most common distribution model (Kumar et al. [22], Bari et al. [1]) is the uniform binary breakage distribution function, (see Eq. (3.66)) which assumes that when one particle breaks, it forms two particles and there is equal probability of forming a particle of any smaller size

$$b(x, x') = \frac{2}{x'}. \tag{3.66}$$

A different approach to the breakage mechanism is described with the ternary distribution. In this case the mother particle forms three particles as described in:

$$b(x, x') = \frac{6}{x'} - \frac{6\,x}{x'^2}. \tag{3.67}$$

Binary parabolic distribution (3.68) and normal distribution (3.69) assume the formation of two particles. The normal distribution is used in the work of Grof et al. [12] for the implementation of a discrete element method (DEM) simulation.

$$b(x, x') = \frac{2}{x'}\left[\frac{6\,x}{x'}\left(1 - \frac{x}{x'}\right)\right], \tag{3.68}$$

$$b(x, x') = \frac{1}{\sigma\sqrt{2\,\pi}} \exp\left[\frac{-(x-\mu)^2}{2\,\sigma^2}\right]. \tag{3.69}$$

A U-Shaped Distribution (3.70) is used in the work of Iggland and Mazzotti [18]

$$b(x,x') = 3\,x^2\,(2q+1)\left(\frac{2}{x'^3}\right)^{(2q+1)}\left(x^3 - \frac{x'^3}{2}\right)^{(2q)}, \tag{3.70}$$

where q denotes the size rate of the produced particles. Large values of q lead to larger difference between the sizes of the two produced crystals. In the case, for example, that $q = 0$, implies the uniform binary daughter distribution function.

An empirical breakage distribution function for multiple breakage introduced from Ziff et al. [71] and it is implemented in the study of Bari et al. [1],

$$b(x,x') = \frac{\varphi\lambda}{x'}\left(\frac{x}{x'}\right)^{\lambda-2} + (1-\varphi)\frac{\eta}{x'}\left(\frac{x}{x'}\right)^{\eta-2}. \tag{3.71}$$

The graphical representation of the different distribution curves are illustrated in Figure 3.4.

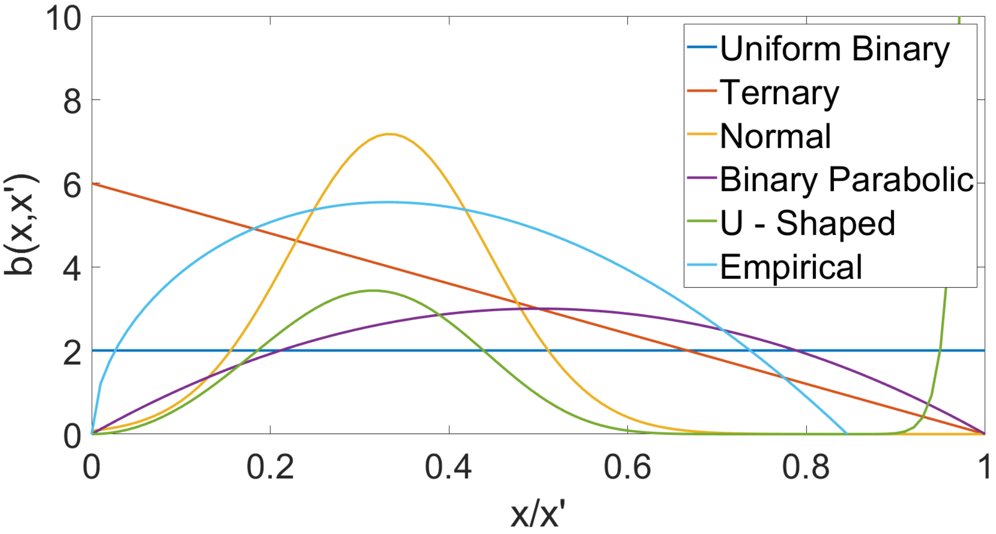

Figure 3.4: Particle size distributions of daughter particles for various distribution functions.

3.5 Optimization Algorithm

The cell average technique allows simulating the number distribution up to a given time for a given breakage rate and daughter distribution. Depending on the selection of the $b(x,x')$ and $S(x)$ the model requires the assumption of the kinetic parameters and the daughter distribution variables respectively when it is needed. Consequently, the breakage parameters S_1 and m in Eq. (3.54) are the optimization design variables, where S_1 depends on the ultrasound power P and the parameter n according to equation (3.55). In the case that i.e. the empirical daughter distribution (3.71) is modeled, the variables φ, λ and η are also included in the optimization process as design variables. As mentioned in the previous sections, the selection of the aforementioned breakage equations depends on the specificity of the system. Therefore, it is necessary to fit the design variables depending on the corresponding breakage experiments.

Upon the decision of the daughter distribution function, we define a cost function, which has to be minimized over experimental measurements in order to estimate the optimum design variables. An optimization algorithm can be used to achieve it. A general optimization technique demands the initialization of the design variables. At each optimization cycle, the design variables are evaluated upon a specific norm. The procedure is repeated until a convergence criterion is satisfied. The convergence rate usually depends on the optimization method. The cost function that is minimized is defined in:

$$f(x) = \frac{1}{T}\frac{1}{N}\sum_{j=1}^{T}\sum_{i=1}^{N} w_{ij}\sqrt{\left(X_{ij}\{exp\} - X_{ij}\{sim\}\right)^2}, \tag{3.72}$$

where T and N denote the time steps and the total nodes, respectively. The $w_{i,j}$ is a weight distribution function and $X_{ij}\{exp\}$, $X_{ij}\{sim\}$ denote the experimental and the simulation results, respectively.

One common convergence criterion is

$$|f(x)^n - f(x)^{n-1}| < r, \tag{3.73}$$

where $f(x)$ stands for the cost function at the optimization cycles n and $n-1$ respectively and r is a post-defined tolerance value.

The selection of the X_{ij} data in Eq. (3.72) is significant and it determines the optimization result. One possible option in the case of breakage would be to fit any of the moments of the distribution. For the moment d_{10} this would mean that the program tries to fit the average volume or size of the particles from the simulation with the experiment. This could lead to a nice match between data and experiment for the moment without the actual number density distributions matching. On the other hand, the cumulative distributions can be considered as a different criterion to fit the experimental data. A more representative criterion and the one used in this work is to fit the entire number density distributions.

The selection of the appropriate optimization algorithm has an important impact on the accuracy of the results and in the computational cost. There are a few studies like Fytopoulos et al. [11] and Grof et al. [12] that approach the objective function with least-squares methods. Furthermore, Mahoney et al. [36] use non-linear optimization in their study. A different approach can be achieved with a generalized cost function for the optimization algorithm as described in Eq. (3.72). In this work, the downhill simplex method proposed by Nelder and Mead [42] is implemented. To achieve the optimum fitting with the experimental results the weight distribution in (3.72) uses the experimental data as it is. A different approach could neglect the weight terms, but due to the nature of the system, i.e in the number density fitting due to the fact that many values are near zero, the results tend to be more accurate using the experimental measurements as weight functions $w_{i,j} = X_{ij}\{exp\}$.

In order to avoid the solution becoming entrapped in local minimum in the optimization procedure, the algorithm has to be performed for different initial values sets. For the initialization of the fitting variables, we used a large interval, linearly discretized. The purpose is to choose random values for every initial set of the design variables. In each optimization case, we used 100 different initial sets. In Figure 3.5 we illustrate the case that only the kinetic parameters S_1 and m need to be fitted.

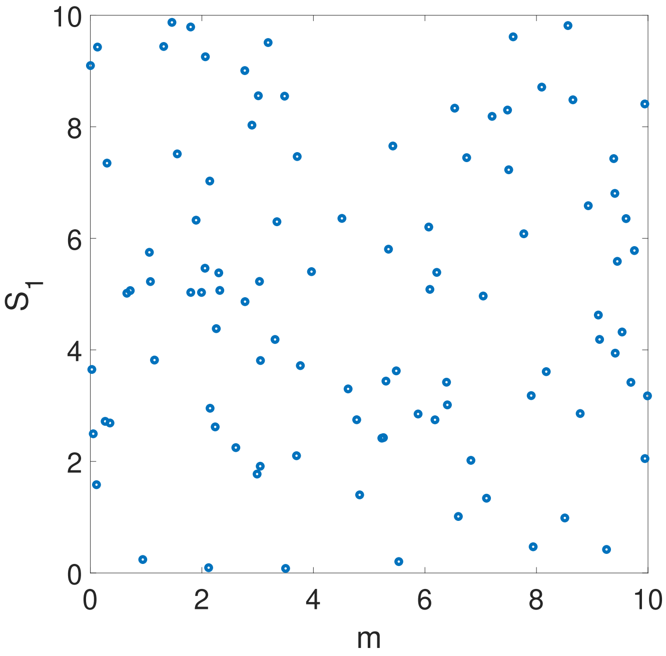

Figure 3.5: Initial sets of values S_1 and m for the optimization algorithm.

Thus, according to Figure 3.5, the selection of the values is completely random in order to avoid possible local minimum values in our solution. The case when the kinetic parameters are the only one degrees of freedom (DOF) is the less expensive referred to computational cost. There are need about 5 hours to run 100 different initial sets on a personal computer in this case. However, in the case that, for example, the empirical daughter distribution (3.71) is modeled, the fitting variables are 5, and the algorithm needs to calculate the integral of Eq. (3.65) in every evaluation. Therefore, the computational cost is largely increased. Consequently, the optimization algorithm is developed to run in parallel in a cluster. The necessary parallel executions were performed in the "Andromeda" cluster of the School of Chemical Engineering, NTUA.

4 Materials and Experimental set-up

In this section are discussed the materials that are used for the ultrasound experiments, as well as the experimental set-up and the procedure, are represented. All the different experiments took place in KU Leuven by professor Georgios Stefanidis and Dr. Xiouras Christos. There is no involvement with the experimental procedure in this work. The results of the experiments are used exclusively in order to fit the kinetic parameters to the CAT method.

4.1 Materials

The sodium chlorate $NaClO_3$ is the key substance for the experiments of this application. Viedma [63] used a saturated solution of sodium chlorate $NaClO_3$ in his study. Sodium chlorate does not have chirality when dissolved but does form chiral crystals. The study included the first experiment to induce homochirality and chiral purity from an initial system where both enantiomers were present through crystallization. In earlier studies, chiral purity was only achieved by seeding the solution. To verify whether ultrasound shows the same results regardless of the chosen compound the same experiment is now performed with L glutamic acid, LGLu.

4.2 Experimental Set-up

The experiment focused on crystal breaking using ultrasound and measuring the crystal size distributions over time while excluding (as much as possible) all other possible particulate events. This is coined pure breakage. The experimental set-up is shown in Figure 4.1. The set-up has a jacketed glass cylinder without lids and an ultrasound transducer. The transducer is positioned at the bottom of the vessel and was made to properly seal the vessel. Utilizing different transducers allows to vary the ultrasound frequency. The temperature of the solution was fixed at $22 \pm 2\,^oC$ by a Lauda thermostatic bath. The temperature is continuously measured by a probe in the solution. To prevent sedimentation of the particles and to allow for representative sampling an axial blade impeller was used as a stirrer. The stirrer operated at around 800 rpm, this speed prevents sedimentation and does not cause particle breakage (verified by an experiment without ultrasound). A waveform generator connected to a power amplifier controls both the frequency and power of the transducers.

4.3 Experimental Procedure

The reactor is filled with a filtered 100 ml solution of Hexane. In the next step ultrasound and stirring are applied which leads to a temporary increase in the temperature. After the temperature stabilized 20 g of Sodium Chlorate crystals $NaClO_3$ was added to the solution. The Hexane acts as an anti-solvent this inhibits other particulate events. At this point, samples are taken with a pipette. These were sent straight to the Malvern 3000 Master-sizer laser diffractometer which measures the crystal size and a Philips XL 30 FEG scanning electron

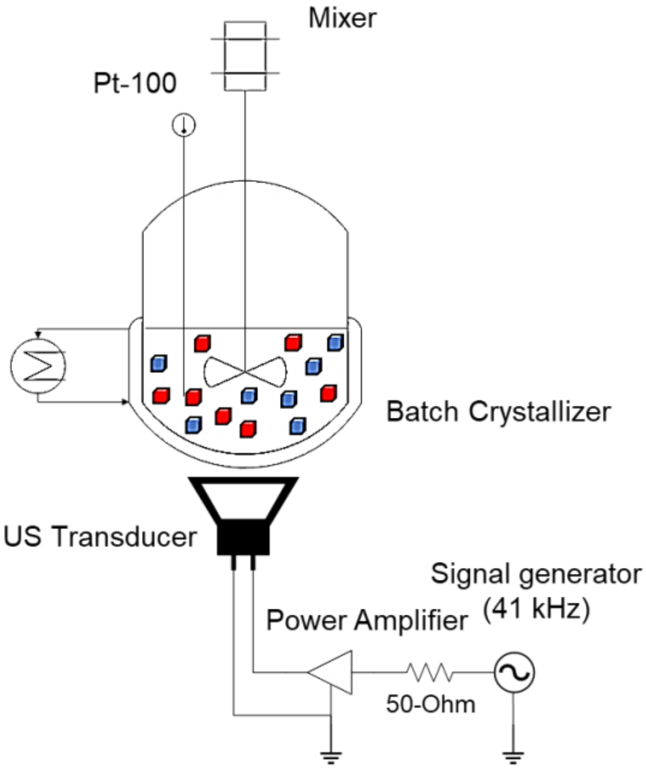

Figure 4.1: Ultrasound breakage experimental set-up [68].

microscope analyzes the crystal shape. Furthermore, 1 gr of lecithin, a surfactant, was added to the solution to prevent the adhesion of crystal particles to the cell window of the Master-sizer.

5 Results

The main purpose of this work is to fit the CAT model in the experimental measurements that took place in KU Leuven by professor Georgios Stefanidis and Dr. Christos Xiouras. It is though important to first validate our code against PBEs with analytic solutions.

5.1 Analytic Solutions of PBEs comparing with CAT

In this paragraph, we compare the results obtained from the implementation of the CAT method for simplified PBEs with known analytic solutions. Consequently, this section aims to test the method and discuss some basic computational aspects.

This application concerns analytical expressions that are proposed by Kumar et al. [23].

The breakage rate is expressed with a power law equation

$$S(x) = x^3. \tag{5.1}$$

A symmetric fragmentation daughter distribution is modeled

$$b(x, x') = \frac{6x^2}{x'^3}. \tag{5.2}$$

The initial particle distribution is given by

$$n_0(x) = 3\,x^2 \frac{N_0}{v_0} exp\left(-\frac{x^3}{v_0}\right), \tag{5.3}$$

where, $N_0 = 1\,m^{-3}$ and $v_0 = 1\,m^{-3}$.

The analytic solution that is proposed by Kumar et al. [23] is

$$n(L, t) = 3\,x^2\,e^{-x^3(1+t)}(1+t)^2. \tag{5.4}$$

For this application, a fine grid of 101 nodes is used. The results concern the initial particle size distribution (PSD) and the 5 time-steps are displayed in Figure 5.1.

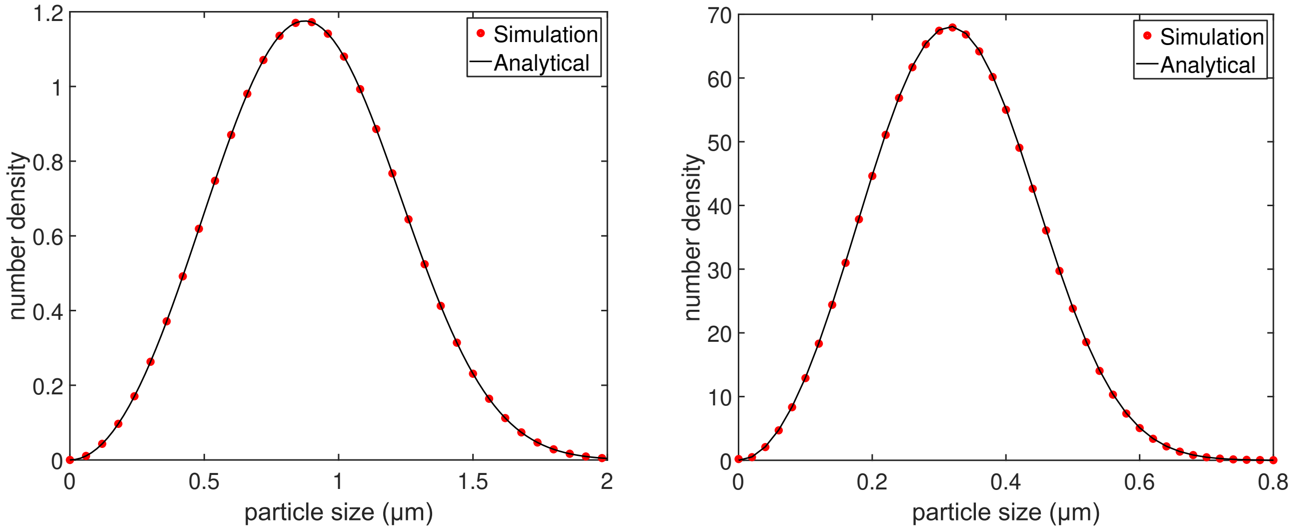

(a) $t = 0\,sec.$ (b) $t = 20\,sec.$

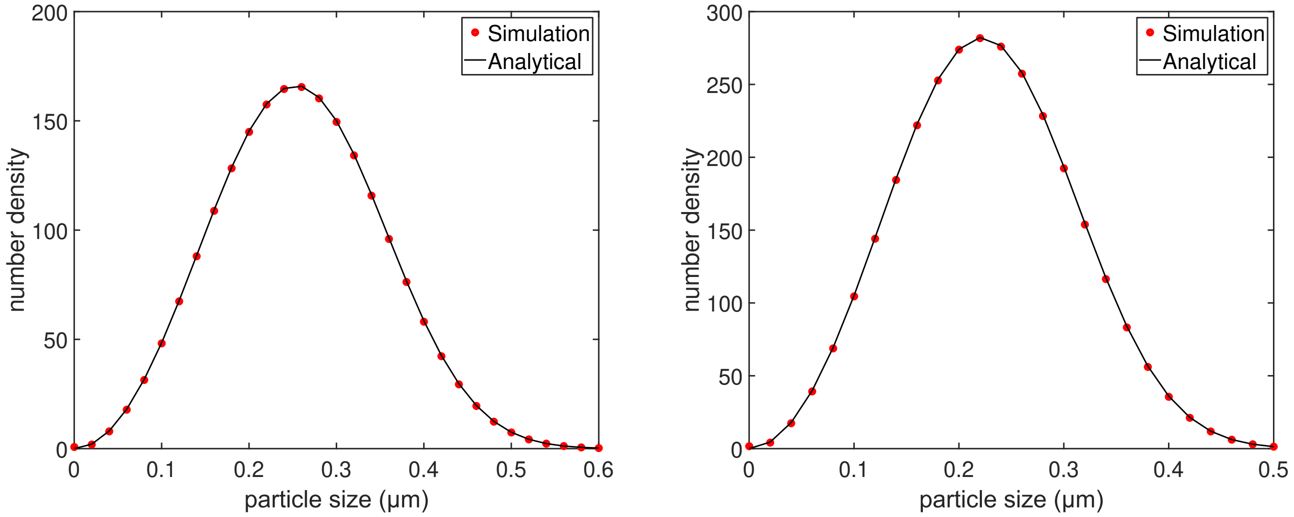

(c) $t = 40\,sec.$ (d) $t = 60\,sec.$

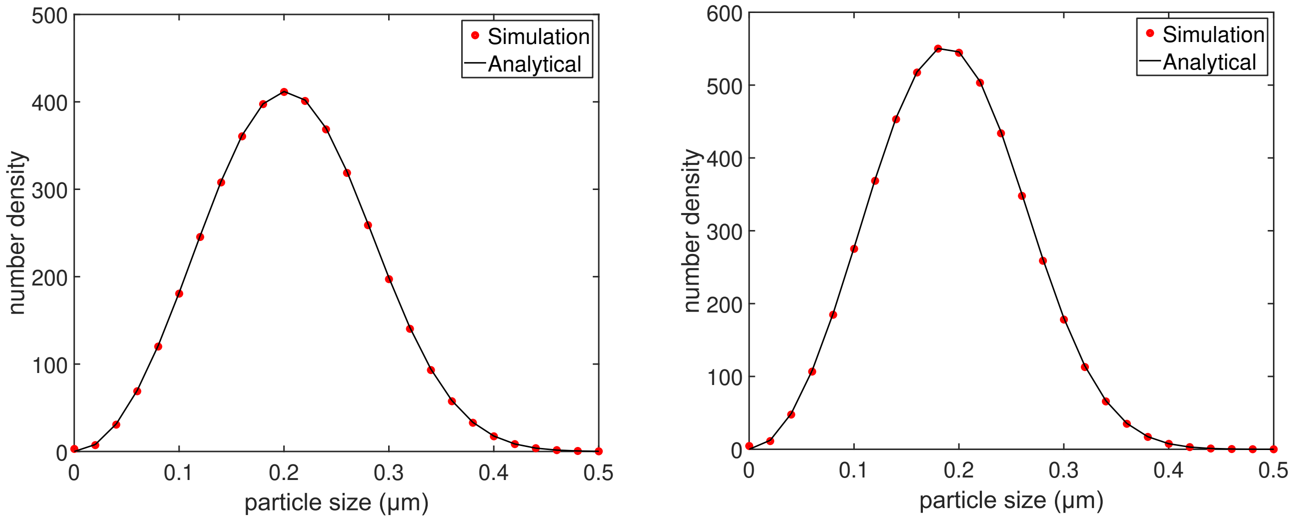

(e) $t = 80\,sec.$ (f) $t = 100\,sec.$

Figure 5.1: Comparison of CAT method with analytic solution Eq. (5.4).

5.2 Simulation of ultrasound breakage experiment

In this section, there are examined the results of different parameters. More precisely, the effects of various kinetic constants, distribution parameters and optimization methods are discussed. For this application is used the reference case of 40 W power and 41 kHz frequency of ultrasound. The comparison of this case with the experimental results is analyzed thoroughly in the next sections.

The grid that is used for the CAT implementation is discretized based on the experimental measurements. The set-up is tuned to capture 100 points of different particle sizes. Thus, the algorithm uses this particle size discretization as it is.

In Figure 5.2 the grid generation is presented.

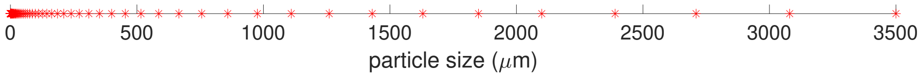

Figure 5.2: Grid generation according to experimental measurements. The particle sizes are depicted in linear scale. The total number of nodes is 100.

The crystal size distribution (CSD), usually is represented either as number or volume distribution. In Figure 5.3 the corresponding number and volume distributions are depicted. These distributions are derived from the experimental measurements. In this study, the number density is used as the initial size distribution in the CAT algorithm. In every distribution, the x-axis is presented in the log scale.

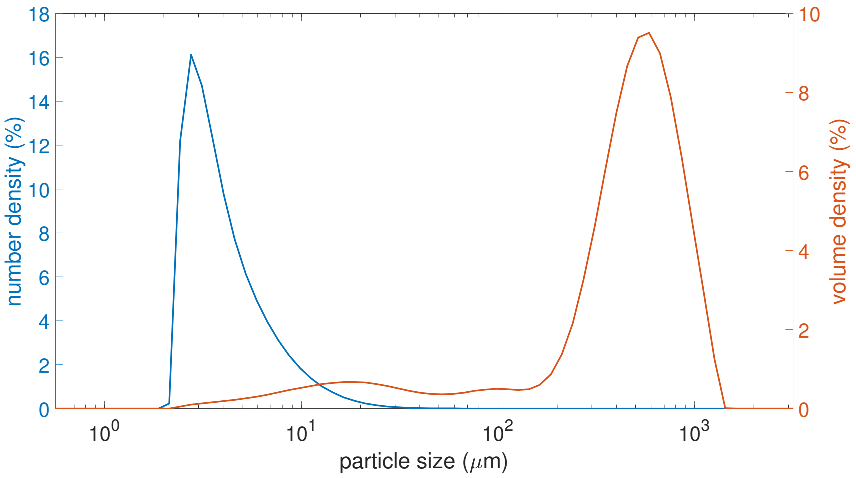

Figure 5.3: Number density and volume distributions of the initial CSD.

5.2.1 Effect of kinetic parameters

In this paragraph, we study the effect of the kinetic parameters S_1 and m when Eq. (3.54), $S(x) = S_1 x^m$ is used. The grid of the reference case of 40 W and 41 kHz is used, but focusing only on the impact of the breakage parameters.

In Figure 5.4 we show the different curves when the S_1 and m parameters change. This is for the case of binary parabolic daughter distribution for $t = 3300\,sec$. In these cases, the parameters are not optimum and the fitting algorithm is not used at all.

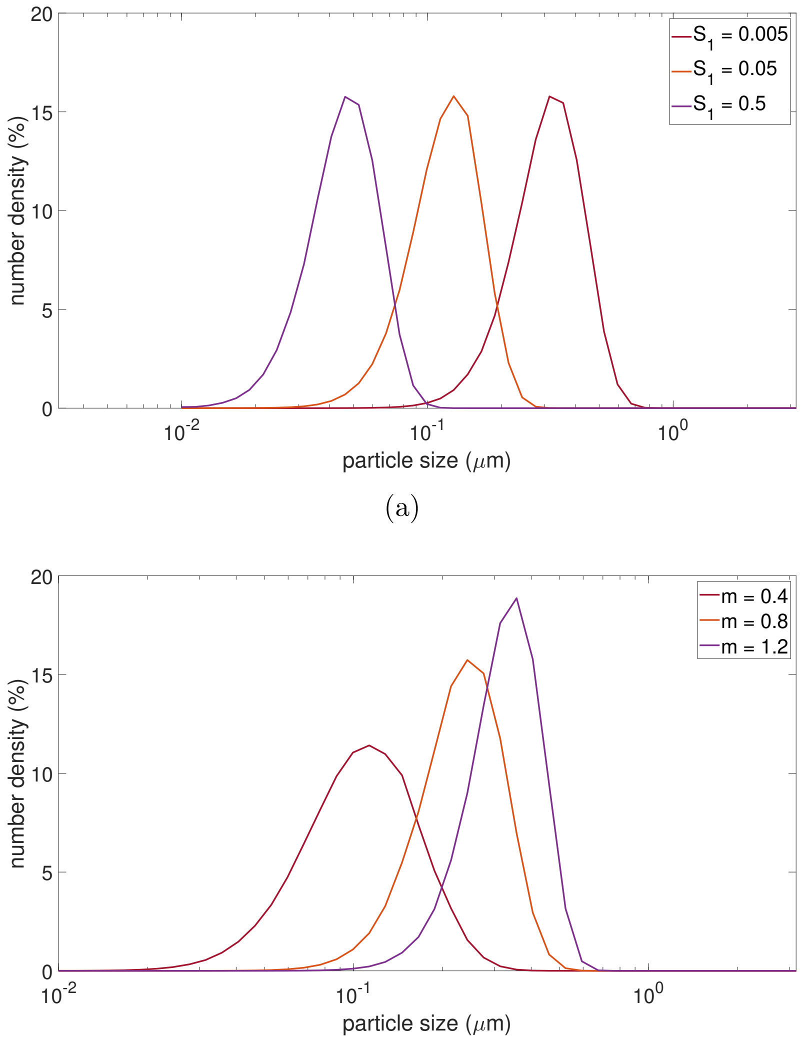

(a)

(b)

Figure 5.4: (a) Effect of S_1 parameter on breakage rate, while the exponential factor is constant and equal with $m = 0.8$. (b) Effect of m exponential factor on breakage rate, while the kinetic parameter S_1 is constant and equal with $S_1 = 0.01$. The binary parabolic daughter distribution is used in both figures.

According to Figure 5.4a, the S_1 parameter has an important impact on the average particle size, while the shape of the number density distribution is not significantly affected. At every size of the crystal, a higher S_1 value results in increased breakage rates. Overall, this indicates that the breakage is occurring more quickly. As the distribution moves to smaller crystal sizes when S_1 increases. The effect of the m kinetic factor is different than S_1, as expected. The results, 5.4b in Figure show that the larger the exponent, the narrower the crystal size distribution becomes. This is due to the fact that a greater exponent for a given crystal size leads to faster breakage. As a result of the low exponent, some particles are not shattered, resulting in a larger spread.

5.2.2 Daughter distribution parameters

In this paragraph, we examine the effect of the parameters used in various daughter distribution functions. There are equations, like binary, binary parabolic and ternary which do not depend on any additional parameter. However, in the case, for example, of the U-shaped daughter distribution (3.70), the q factor is a design variable , likewise the φ, λ and η parameters of empirical equation (3.71). Additionally, in normal function the mean value μ as well as the standard deviation σ affect the overall form of distribution in Eq. (3.69).

U-Shaped Distribution

For the case of U-shaped distribution, we first study the effect of q and present representative results in Figure 5.5. The figure shows the simulated number density function at time, $t = 3300\,sec$. The kinetic parameters remain constant for the various q values and they are $S_1 = 0.01$ and $m = 1.1$.

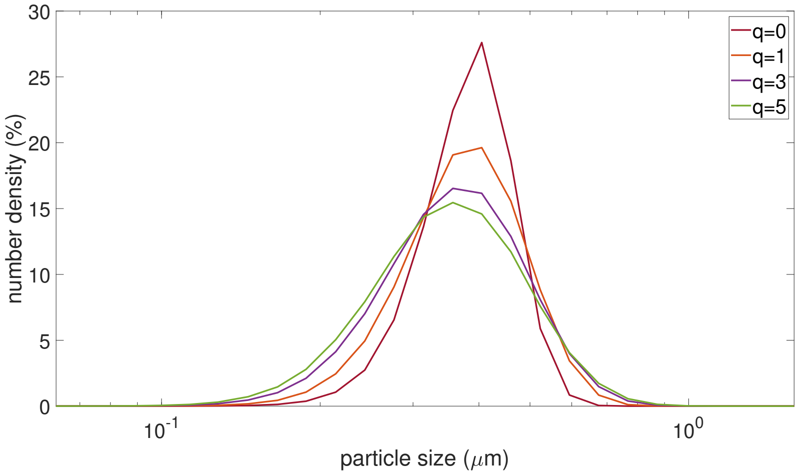

Figure 5.5: Comparison of different q values for U-shaped distribution after time, $t = 3300\,sec$ and constant kinetic parameters, $S_1 = 0.01$ and $m = 1.1$.

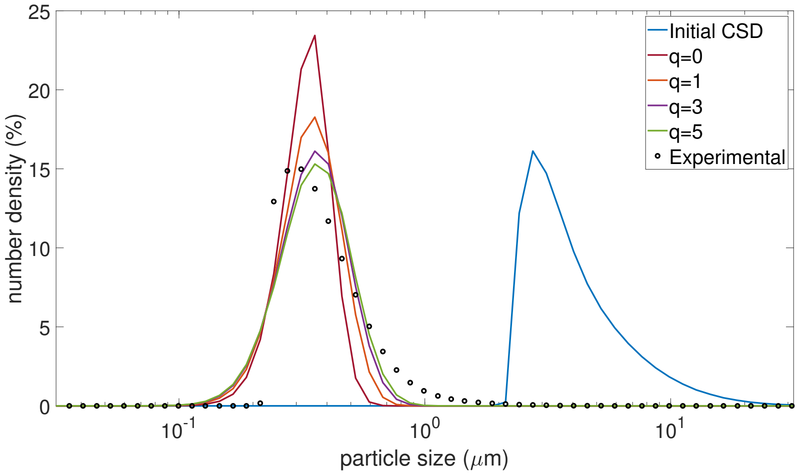

Figure 5.6: Best fitting obtained for different q values when the U-shaped daughter distribution function is used. Fitting is performed to fit S_1 and m values for each q value.

Figure 5.6 presents the best fitting distributions to the experimental one obtained at time, $t = 3300\,sec$. In particular, we fit S_1 and m values using the U-shaped distribution function and different q values. Therefore, for the latter case, the optimization algorithm as described is chapter 3.5 is needed. The weight functions in Eq. (3.72) are not taken into account in this case.

The optimized kinetic parameters, as well as the minimum values of the cost function Eq. (3.72) are presented in Table 1.

Case	Kinetic Parameters S_1	m	q	$min\, f(x)$
1	$8.292352 \cdot 10^{-3}$	0.780062	$q = 0$	$8.165538 \cdot 10^{-3}$
2	$9.159949 \cdot 10^{-3}$	0.902879	$q = 1$	$3.567647 \cdot 10^{-3}$
3	$9.207230 \cdot 10^{-3}$	1.015681	$q = 3$	$2.717376 \cdot 10^{-3}$
4	$9.180562 \cdot 10^{-3}$	1.082230	$q = 5$	$2.589753 \cdot 10^{-3}$

Table 1: Optimization results referred to minimization of Eq. (3.72) for different q values of U-shaped (3.70) distribution.

As expected, there are important differences referred to the values of the q rate. The optimum minimization of the objective function (3.72) is achieved for q equal to 5. The q in U-shaped distribution affects the sizes of the two produced crystals. Therefore, the larger its value, the more important the size difference between the two developed particles. As a result, the value of $q = 5$ is representative for the system that is studied.

Empirical Distribution

This distribution is a multi-breakage daughter distribution with three different design variables, φ, λ and η. Generally, the breakage of a crystal leads to the formation of at least two particles. The distributions that are discussed in this thesis, usually model the creation of two particles. The ternary equation is an exception, since it creates three particles. The empirical distribution (3.71), theoretically can form multiple particles. Therefore, when the empirical distribution is used we need to take into account a physical restriction concerning the average number of particles produced in a fragmentation event, N_p, which is described by (5.5)

$$N_p = \int_0^{x'} b(x, x')\, \mathrm{d}x' \geq 2. \tag{5.5}$$

The restriction of equation (5.5) can be converted into a simplified inequality function in terms of the requested parameters [71].

$$\frac{\lambda\eta - \varphi\lambda - (1-\varphi)\eta}{(\lambda - 1)(\eta - 1)} \geq 2 \tag{5.6}$$

In Figure 5.7 we plot the simulated number density function at times $t = 3300$ and $5700\, sec$ when two optimization scenarios are considered. One, that produces optimal parameter values neglecting restriction (5.6) and one that performs fitting taking into account this restriction. The corresponding fitting results are presented in Table 2. In the optimization algorithm a weight distribution has been used, denoted as $w_{i,j} = X_{ij}\{exp\}$.

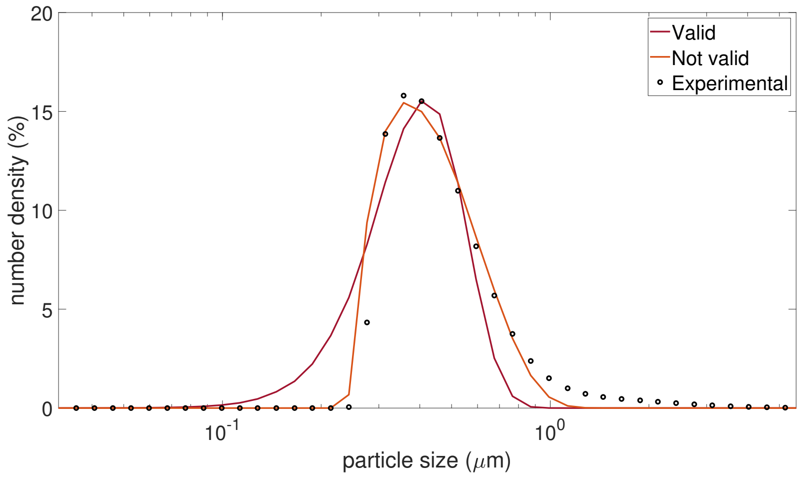

(a)

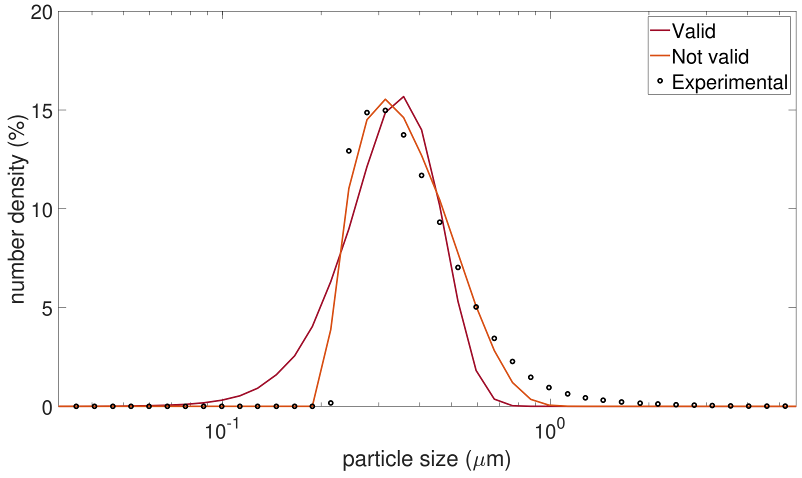

(b)

Figure 5.7: Comparison of optimized number density distribution functions using the empirical daughter distribution function. The red and orange lines correspond to optimization taking and neglecting the restriction (5.6), respectively. (a) Results after $t = 3300\,sec$ and (b) Results after $t = 5700\,sec$.

It is obvious that when there is no constraint in the daughter distribution, the optimization algorithm can fit the three parameters in the best way. Of course, this violates the physical restriction described in Eq. (5.6). Therefore, this solution is not acceptable and it is presented only to realize a possible failure in this system.

Case	Method	Kinetic Parameters		Distribution Parameters			$min\,f(x)$
		S_1	m	λ	φ	η	
1	Valid	$2.217846 \cdot 10^{-3}$	1.129691	5.487047	2.530262	3.880954	$5.380825 \cdot 10^{-3}$
2	Not Valid	$0.869836 \cdot 10^{-3}$	1.078713	5.571597	0.386295	0.240043	$3.405115 \cdot 10^{-3}$

Table 2: Optimization results referred to minimization of Eq. (3.72). We present two scenarios of optimization: one which takes into account the restriction Eq. (5.6) and one that neglects the restriction.

The optimization aspects concerning the fitting for the U-shaped and empirical distributions are analyzed in the next chapter.

5.2.3 Optimization specifications

As mentioned in paragraph 3.5, there is the need for an optimization method to estimate the kinetic parameters and the distribution characteristics (when it is needed) for the system that is modeled. In this work, the downhill simplex method proposed by Nelder and Mead [42] is used. We also perform a comparison between the simplex method and a non-linear least-squares technique is made for the sake of completeness. It is important to note that the requested optimum parameters concern the entire application, thus the fitting process refers to all the corresponding time steps.

For this test, the binary parabolic and the U-shaped distributions are used. In the first case the weights distribution on (3.72) is $w_{i,j} = 1$, i.e. they have no any impact in the cost function.

Figure 5.8 illustrates a comparison of simplex (FMS) and non linear least squares (NLS) methods for binary parabolic (3.66) and U-shaped (3.70) distributions at $t = 3300\,sec$ from the start of the experiment. For the U-shaped distribution we set $q = 5$.

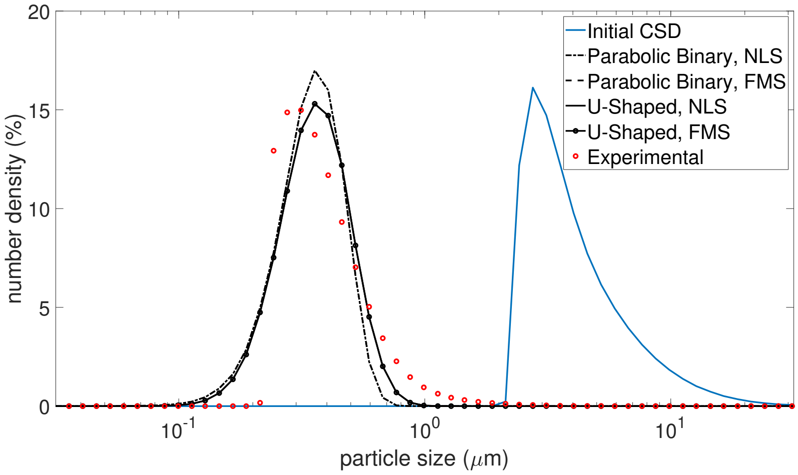

Figure 5.8: Number density distributions. Differences between simplex (FMN) and non linear least squares (NLS) methods for binary parabolic and U-shaped distributions at $t = 3300\,sec$.

The results referred to the comparison of the optimization techniques are identified as expected. However, both methods have deviations compared to experimental measurements. The treatment, as well as the optimum algorithm for the system that is modeled, will be examined in the next chapters.

In Table 3 we report the calculations of the two algorithms. The two fitting methods provide almost equal results. The initialization is significant in order to achieve the global solution. It has been pointed out that the algorithm uses 100 different initial sets in order to estimate the global minimum. The initialization that is used in these cases provides the minimum value of the cost function. Thus, it is considered that the solution is not trapped in a local minimum.

In general, the CAT method simulating pure breakage requires about 5 to 7 seconds in a discretized domain of 100 nodes, to simulate 3.5 hours of the experiment. This domain is mainly used in this thesis since it is created according to the experimental measurements which in each case are about the same number. Therefore, the main CPU cost increased in the process of optimization.

Case	Method	Distribution	Kinetic Parameters		$min\, f(x)$
			S_1	m	
1	FMN	Binary Parabolic	$2.951197 \cdot 10^{-3}$	0.948542	$3.547241 \cdot 10^{-3}$
2	NLS	Binary Parabolic	$2.951145 \cdot 10^{-3}$	0.948537	$3.547241 \cdot 10^{-3}$
3	FMN	U-Shaped	$9.180562 \cdot 10^{-3}$	1.082229	$2.589752 \cdot 10^{-3}$
4	NLS	U-Shaped	$9.180565 \cdot 10^{-3}$	1.082230	$2.589752 \cdot 10^{-3}$

Table 3: Optimization results referred to minimization of Eq. (3.72). Comparison of the simplex (FMS) and non linear least squares (NLS) methods methods for binary parabolic and U-shaped distributions.

In Figure 5.9 the computational cost of the optimization of each method referred to the requisite function evaluations is depicted.

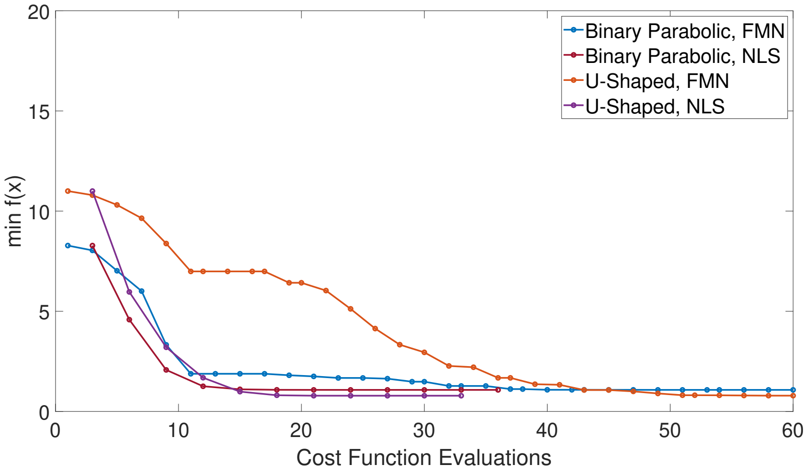

Figure 5.9: Comparison of simplex (FMN) and non linear least squares (NLS) methods for binary parabolic and U-shaped distributions.

According to Figure 5.9, the non-linear least-squares method is way faster than the simplex technique in this case. However, it has been pointed out that the former algorithm is very likely to get trapped in local minimum solutions. Therefore, for this work, as only the crystal breakage mechanism is studied, it is considered that the computational cost of the simplex algorithm is not prohibitive. Furthermore, figure 5.9 concerns a case with specific initialization in the optimization algorithm, which is known beforehand that it has, as a result, the global minimum value. However, in all the cases of this work, it is necessary to define a multi-start algorithm for the initialization of the values, in order to know that the final solution refers to the global minimum. Taking into account all the above remarks, the simplex algorithm is the most appropriate and it is used exclusively in this work.

In Figure 5.10, we illustrate the fitting without and with the weight functions, respectively. Because of the system's design, i.e in the number density fitting, due to the fact that many values are near zero, the algorithm exploits the experimental measurements as weight functions, $w_{i,j} = X_{ij}\{exp\}$.

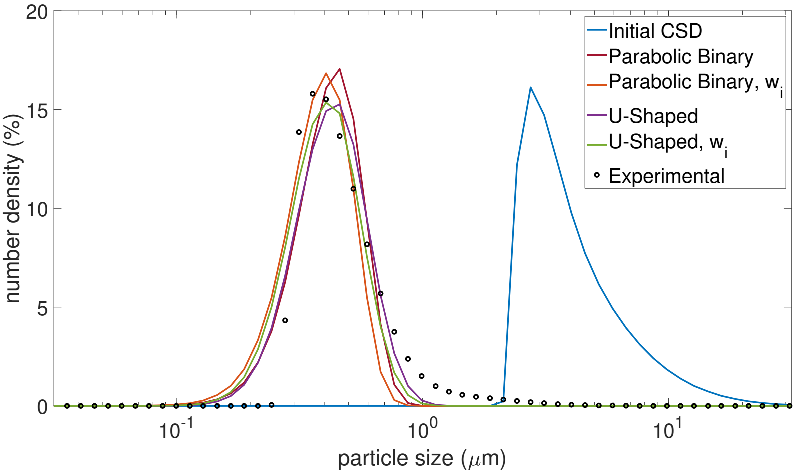

Figure 5.10: Comparison of simplex (FMN) method for binary parabolic (3.66) and U-shaped (3.70) distributions considering weights in Eq. (3.72) at $t = 3300\,sec$.

There are no significant differences with the use of weights in the cost function. The main deviations are observed on the smaller and larger particles, respectively. The use of weight functions takes more into account the smaller and medium-sized particles, while in the case of $w_{i,j} = 1$ the larger particles are simulated better. Therefore, it is considered that the use of weights is more appropriate for this work.

Table 4 illustrates the optimum parameters for the aforementioned cases. The min $f(x)$ values are not comparable, while the corresponding objective functions are reasonably different.

Case	$w_{i,j}$	Distribution	Kinetic Parameters S_1	 m	$min\,f(x)$
1	1	Binary Parabolic	$2.951197 \cdot 10^{-3}$	0.948542	$3.547227 \cdot 10^{-3}$
2	$X_{ij}\{exp\}$	Binary Parabolic	$3.760807 \cdot 10^{-3}$	0.935292	$6.022376 \cdot 10^{-3}$
3	1	U-Shaped	$9.180562 \cdot 10^{-3}$	1.082229	$2.589752 \cdot 10^{-3}$
4	$X_{ij}\{exp\}$	U-Shaped	$11.469618 \cdot 10^{-3}$	1.104574	$4.764838 \cdot 10^{-3}$

Table 4: Optimization results referred to minimization of Eq. (3.72). Differences of using weights in the simplex (FMS) method for binary parabolic (3.66) and U-shaped (3.70) distributions.

One more parameter in the optimization model is the fitting data. It is mentioned that in this work the algorithm uses the number density distributions to fit the experimental data. However, the are studies in the literature where the cumulative distribution data or a specific distribution moment are used.

Thus, figure 5.11 displays a comparison between probability (PDF) and cumulative (CDF) distribution functions for the U-shaped equation. The diagrams refer to time, $t = 3300\,sec$. As expected, the optimization method fits the best the corresponding distribution.

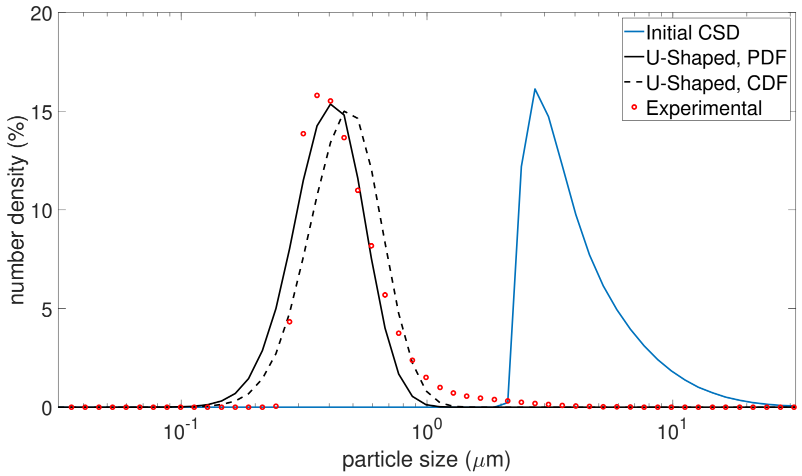

(a) Number density distribution.

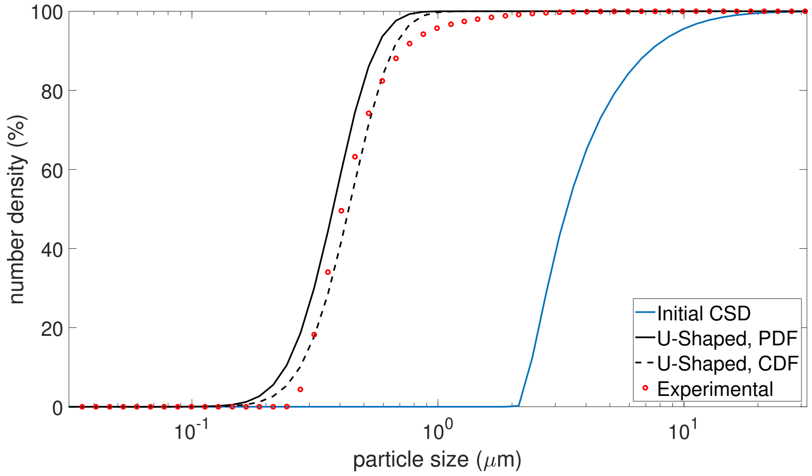

(b) Cumulative distribution function.

Figure 5.11: Number distribution comparison when the fitting algorithm refers to probability or cumulative distribution. Here, the U-shaped distribution is used with $q = 5$.

Table 5 presents the optimum parameters when weight functions are incorporated in the cost function, considering $w_{i,j} = X_{ij}\{exp\}$. In this case the U-shaped distribution is implemented.

Case	Distribution	Kinetic Parameters		$min\ f(x)$
		S_1	m	
1	PDF	$11.469618 \cdot 10^{-3}$	1.104574	$4.764838 \cdot 10^{-3}$
2	CDF	$6.533906 \cdot 10^{-3}$	1.029236	$1.199379 \cdot 10^{-1}$

Table 5: Optimization results referred to minimization of Eq. (3.72). Differences between using probability (PDF) and cumulative (CDF) distributions in optimization algorithm.

In this case, also, the optimization results are not comparable, since different data are used.

5.3 Experimental measurements comparing with CAT

5.3.1 Reference Case

The purpose of this paragraph is to define the appropriate daughter distribution function, Eqs. (3.66)-(3.71) in order to simulate ultrasound crystal breakage. The experimental section of the reference case was implemented with an ultrasonic transducer at 40 W and 41 kHz. The laser diffraction meter measures the volume distribution of samples taken at different time steps. Figure 5.12a depicts the results of the comparison of ternary (3.67) and binary parabolic (3.68) distributions with the U-shaped equation (3.70) at $t = 3300\,sec$.

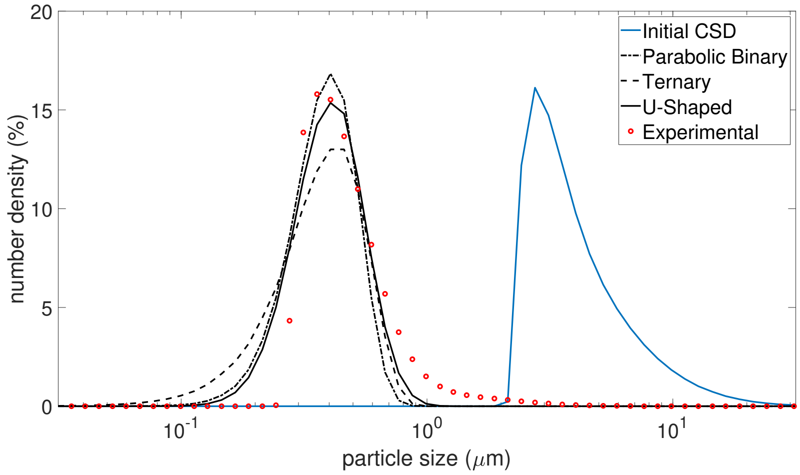

(a) Number density distribution.

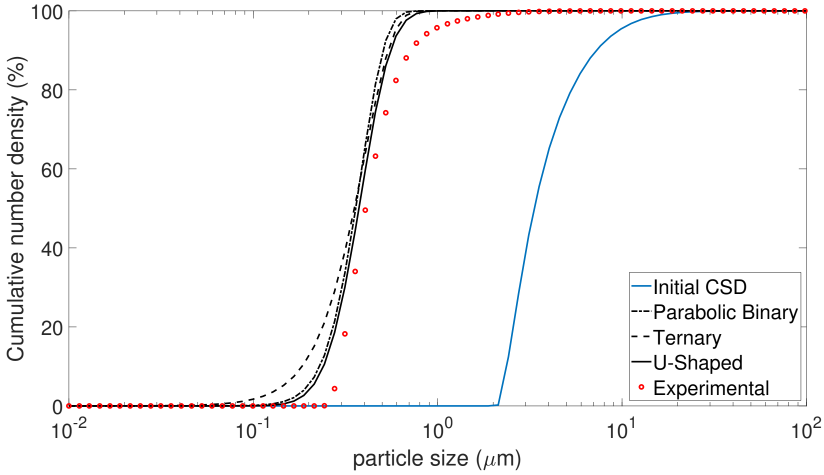

(b) Cumulative distribution function.

Figure 5.12: Comparison of three different daughter distributions with experimental measurements for $t = 3300\,sec$.

Using the U-shaped distribution, in Figure 5.12a the breakage process appears to have different behavior compared to the other daughter distribution function. More specifically, the smaller particles get more negligible influence (i.e. at $10 - 0.5\mu m$), while the effect of bigger particles is greater. The q factor of U-shaped function (3.70) represents the size ratio of the produced particles. Therefore, to achieve the best results, especially concerning the larger particles the

q rate is chosen to be constant and equal with $q = 5$. The influence of the smaller particles in the experimental measurements is not representative enough due to the physical restrictions of the experimental set-up. The same tendencies can be observed in the case of the cumulative distribution function, figure 5.12b, where the U-shaped function can produce better results. As has been pointed out, the optimization algorithm is used directly in the number density distribution, but for the sake of completeness, the cumulative distribution is also displayed.

In Table 6 a complete view for the optimization results of all the daughter distributions that are denoted in subsection 3.4.2 is given. The U-shaped distribution can provide a more accurate fitting for the reference case. Thus, the aforementioned distribution equation is considered to provide the most accurate fitting for the under investigation system and is used extensively in the following sections.

Daughter Distribution		Kinetic Parameters		Distribution Parameters	$min\, f(x)$
		S_1	m		
Uniform Binary	Eq. (3.66)	$3.9 \cdot 10^{-3}$	1.0479	–	$5.9752 \cdot 10^{-3}$
Ternary	Eq. (3.67)	$2.5 \cdot 10^{-3}$	1.2604	–	$6.1145 \cdot 10^{-3}$
Binary Parabolic	Eq. (3.68)	$3.7 \cdot 10^{-3}$	0.9353	–	$6.0224 \cdot 10^{-3}$
Normal	Eq. (3.69)	$7.5 \cdot 10^{-3}$	1.2402	$\mu = 3.8542$, $\sigma = 1.0978$	$5.8656 \cdot 10^{-3}$
U-Shaped	Eq. (3.70)	$11.5 \cdot 10^{-3}$	1.1045	$q = 5.0000$	$4.7646 \cdot 10^{-3}$
Empirical	Eq. (3.71)	$2.2 \cdot 10^{-3}$	1.1296	$\varphi = 5.4870$, $\lambda = 2.5303$, $\eta = 3.8809$	$5.3808 \cdot 10^{-3}$

Table 6: Optimization results referred to minimization of Eq. (3.72). The S_1 and m are the optimum kinetic parameters as described in the Eq. (3.54). The corresponding distribution parameters are defined based on the Eqs. (3.66)-(3.71).

In Figure 5.13 we depict the volume distribution of the produced crystals during the experiment. It can be observed that while smaller and smaller particles are formed over time, the distribution shifts to the left, and over long processing times, the volume of the many small particles balances out the volume of the fewer but larger particles.

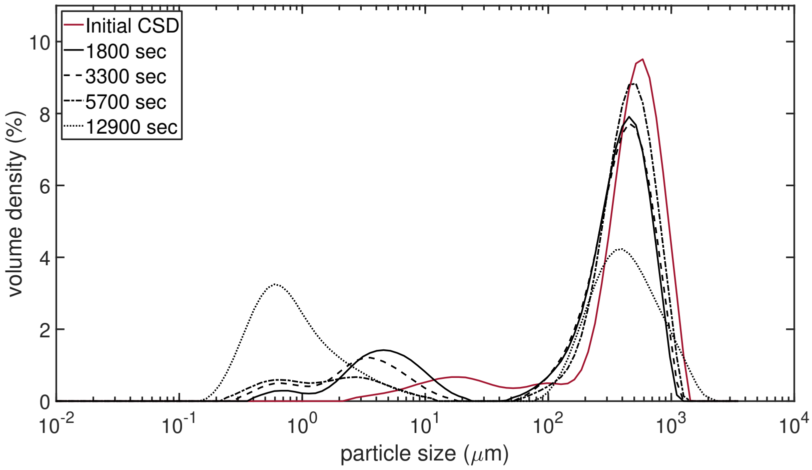

Figure 5.13: Evolution of experimental volume density distribution.

Ultrasound appears to alter the original distribution by inducing new very small particles compared to the original particles. This explains the two peaks in the volume distribution.

The CAT algorithm can calculate the total number of particles as it is defined with Eq. (3.18). The results of the method's implementation for the reference case of ultrasound power of 40 W and frequency stabilized in 41 kHz respectively are illustrated in 5.14a. Due to the fact that the experimental set-up can measure the number densities of the produced particles, in order to compare the method with the measurements, in 5.14b the corresponding number densities distributions are displayed.

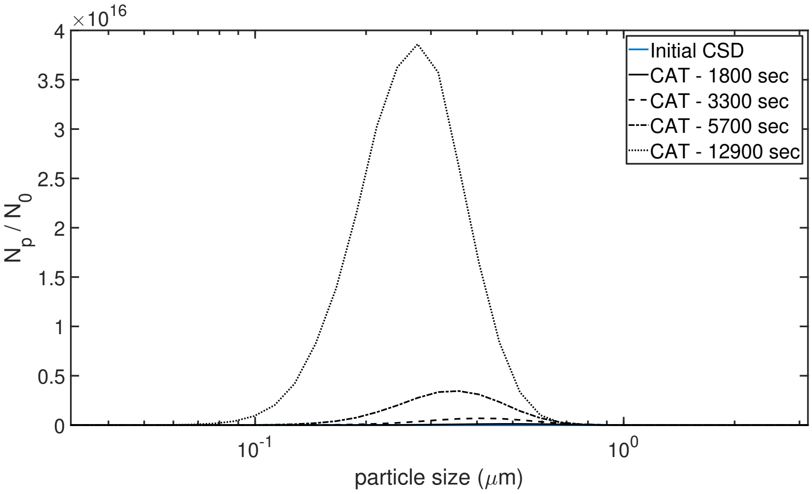

(a)

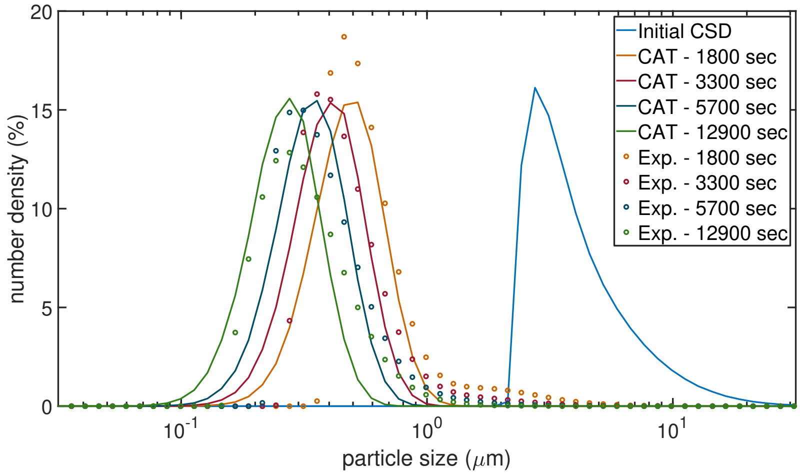

(b)

Figure 5.14: (a) Total number of calculated crystals and (b) The corresponding number density distribution for the reference case of 40 W and 41 kHz.

The model can simulate better the higher crystal concentrations for larger times. In Figures 5.14, it is clear that as time passes smaller particles are formed, thus the distributions in 5.14b shifted to the left as expected. As the crystals break and smaller particles are formed, they are more difficult to continue breaking. This fact is observed in the case of number distributions in Figure 5.14b. In the experimental measurements, smaller particles are produced as time goes on, while in the CAT method the maximum number density remains stable during the simulation. As far as the experiment is concerned, this implies that once crystals reach a certain size, ultrasound can no longer break them, and the model becomes less effective.

As a comparison, d_{10} characteristic diameters can be calculated for both the simulation and the experiment, as shown in Figure 5.15. Similar patterns can be seen in the diameters. The diameters of the experiment distributions are greater than those of the simulations, which is mostly due to the right-hand tail in the experiment number distributions.

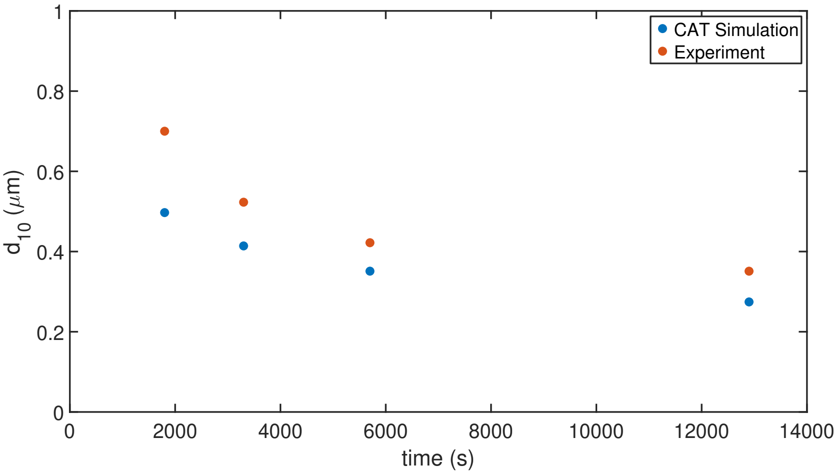

Figure 5.15: Evolution of mean diameter d_{10}.

Using ultrasound grinding leads to relatively large volume particles remaining even after long processing times. The final distribution contains many small particles and a couple of larger particles that balance themselves out in terms of volume.

5.3.2 Ultrasound Power Impact on Crystal Breakage

The ultrasound strength leads to different behaviors on the crystal breakage. In this section, the CAT model uses the U-shaped daughter distribution that is described in Eq. (3.70), combined with the power law breakage rate, Eq. (3.54) in order to describe the effect of ultrasound power. In these cases, the frequency remains constant at 41 kHz and the wattage of the experiments ranges from 20 to 60 W with a step of 20 W.

The results of the CAT model for the combination of 40 W and 41 kHz are thoroughly examined in the previous paragraph. In the case of 20 W, in number density distribution, figure 5.16a the model shows discrepancies for the higher number densities while, even after $t = 5760\,sec$ is difficult to capture the peaks of the distribution. On the other hand, in the cases of 30 and 60 W, figures 5.17a and 5.18a respectively the results are more accurate. More precisely, during the initial time steps, the higher number densities are also difficult to be fitted, but the distribution for the larger particles is calculated more accurately.

As far as the volume densities are concerned some common tendencies between the different cases of ultrasound power can be observed. More precisely, in the cases of 40 W and 60 W, there are similarities in the shape of the curves, as well as in the peaks that are created from the smaller particles, when the time steps are close. In the case of 30 W of power, the impact of smaller particles is more significant compared to the other three cases. On the other hand, in the volume distribution in the case of 20 W, the left peak is more negligible, while the right top is noticeably important. In the latter case, the power of ultrasound seems to be weak to break an important amount of larger particles that remain after a long time.

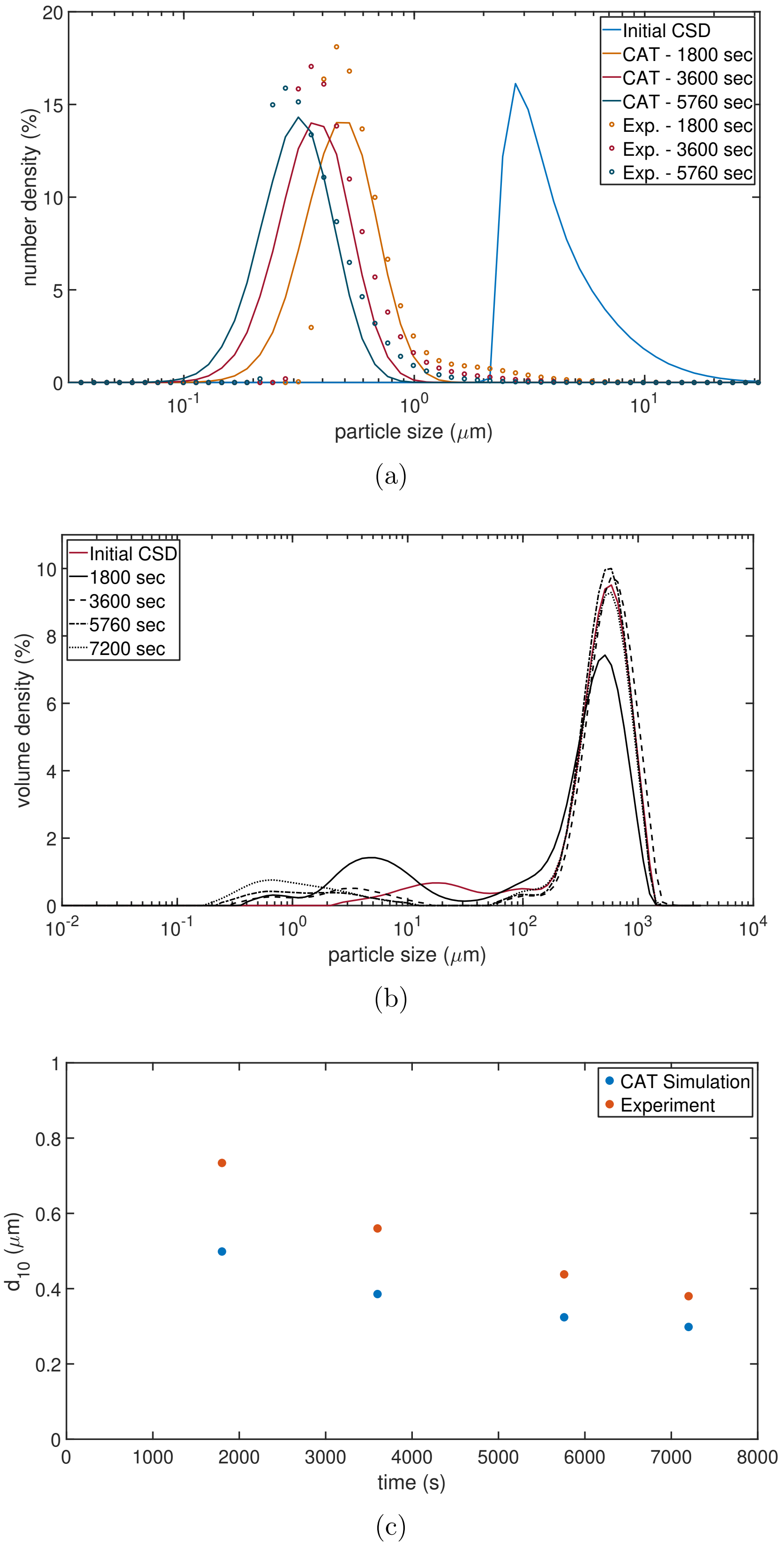

Figure 5.16: (a) Snapshots of number density distribution function, (b) The corresponding experimental volume density distribution and (c) The d_{10} mean diameter for the 1^{st} case of 20 W and 41 kHz.

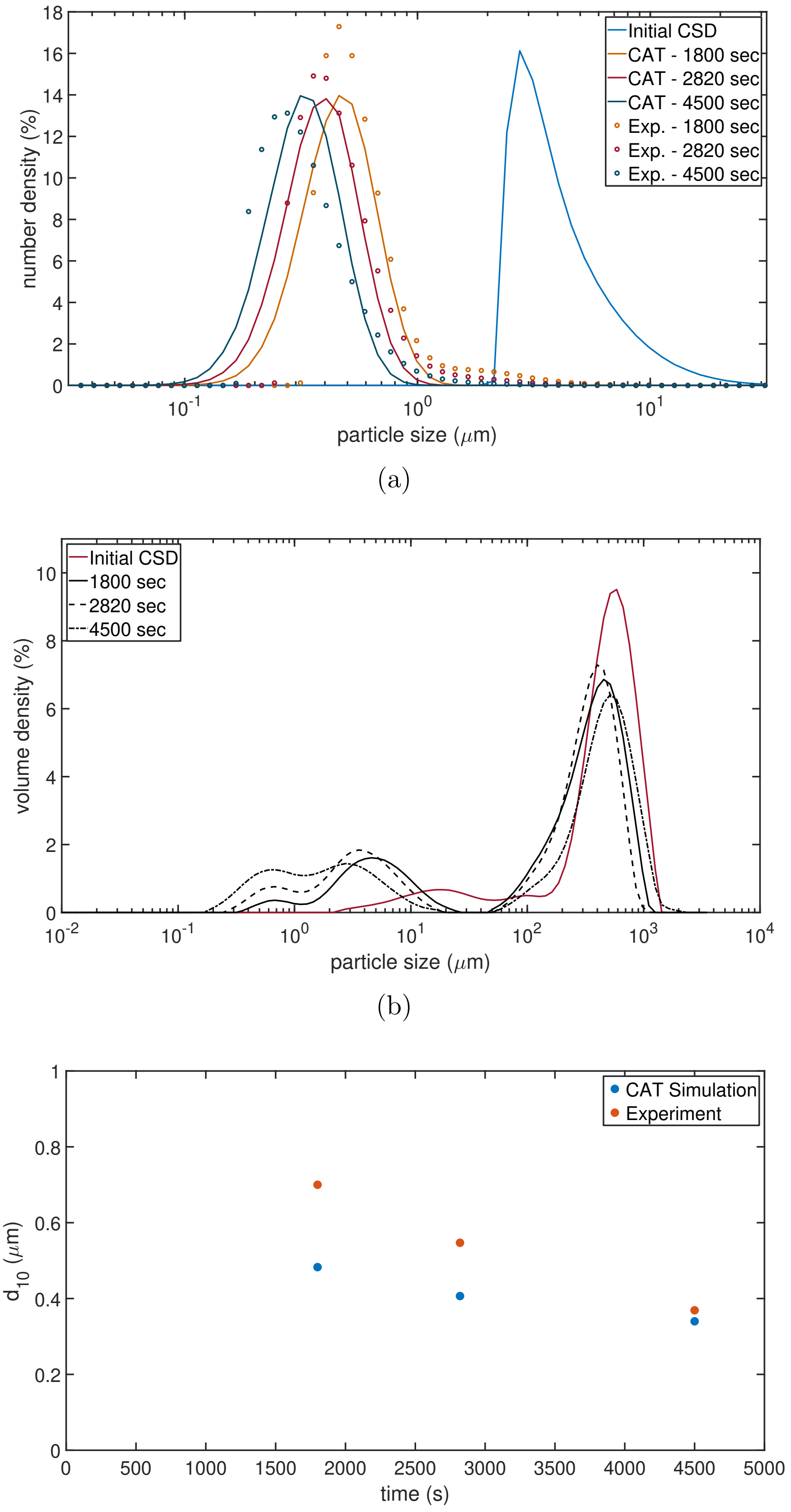

(a)

(b)

(c)

Figure 5.17: (a) Snapshots of number density distribution function, (b) The corresponding experimental volume density distribution and (c) The d_{10} mean diameter for the 2^{nd} case of 30 W and 41 kHz.

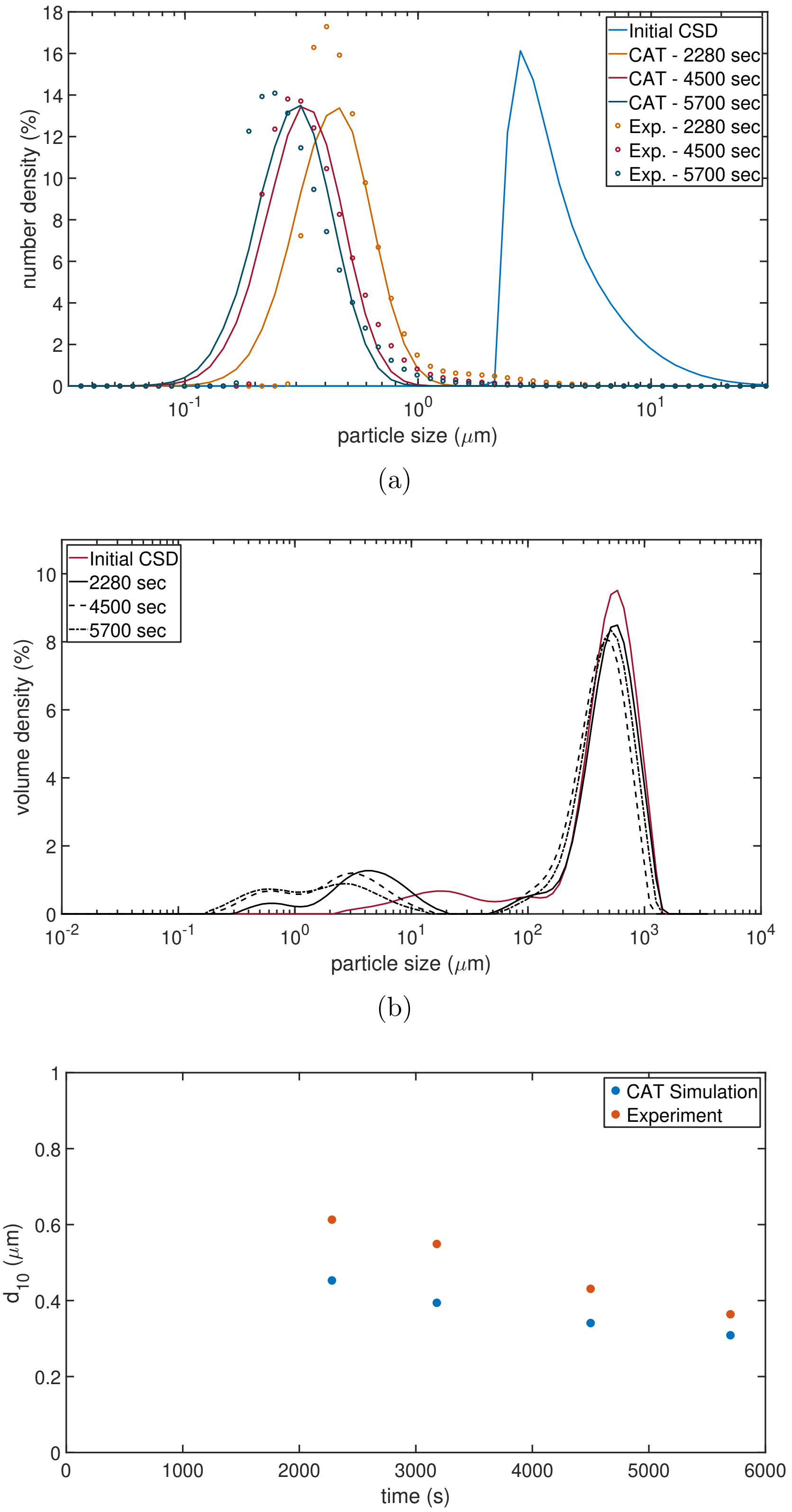

(a)

(b)

(c)

Figure 5.18: (a) Snapshots of number density distribution function, (b) The corresponding experimental volume density distribution and (c) The d_{10} mean diameter for the 4$^{\text{rth}}$ case of 60 W and 41 kHz.

Generally, despite small deviations, the model results tend to follow the experimental number densities of both the small and the larger particles after about the first hour of simulation. In the case of 60 W 5.18a, the CAT simulation after 75 min provides the best results, compared to the experimental measurements. The model of 30 W 5.17a appears some variations, while the best fitting concerns the second time step of the experiment, i.e. about 47 min after the start of the experiment. In general, the fitting of the parameters is done over all the time steps of the experimental measurements. As a result, the simulation is not able to capture the peak of the number density distribution in the first (or even in the last, in some cases) time step accurately. Furthermore, even though we use weight functions in the optimization algorithm, there are few experimental measurements (about 20 different points can form the "bell curve") in the number density distribution that are significantly greater than zero. Therefore, it is difficult to approach the peak of the number density distribution in the initial time measurements. This conclusion applies in all the cases that we fit the CAT method to experimental results in this thesis.

Case	Power (W)	Frequency (kHz)	Kinetic Parameters		$min\, f(x)$
			S_1	m	
1	20.0	41.0	$10.04 \cdot 10^{-3}$	0.8990	$5.2006 \cdot 10^{-3}$
2	30.0	41.0	$10.78 \cdot 10^{-3}$	0.8707	$4.3013 \cdot 10^{-3}$
3	40.0	41.0	$11.50 \cdot 10^{-3}$	1.1045	$4.7646 \cdot 10^{-3}$
4	60.0	41.0	$9.55 \cdot 10^{-3}$	0.7969	$4.4851 \cdot 10^{-3}$

Table 7: Optimization results referred to minimization of Eq. (3.72). The S_1 and m are the optimum kinetic parameters as described in the Eq. (3.54). For all these cases the produced particle rate $q = 5$.

The measurements of the 20, 30, 40 and 60 W experiments indicate that the ultrasound power initially has a large influence, but it becomes less effective during the process. Table 7 reports the optimum kinetic parameters for the different ultrasound power values. The case of 30 W power gives the minimum $f(x)$, while the biggest deviation from the experiment appears for the 20 W experiment. The mean diameters d_{10}, also appear similarities during the wattage increase. Specifically, as time passes, the fitting of these values is more accurate.

In Figure 5.19, the fitting model is represented by a power law function as it is defined in Eq. (5.7). The optimum parameters of the power law for ultrasound strength increase are shown in Table 8.

$$S(P) = S_1 P^n \tag{5.7}$$

$S(P)$ Coefficients	Value
S_1	$7.2050 \cdot 10^{-3}$
n	$1.0730 \cdot 10^{-1}$

Table 8: Optimum kinetic parameter of the fitted power law $S(P)$.

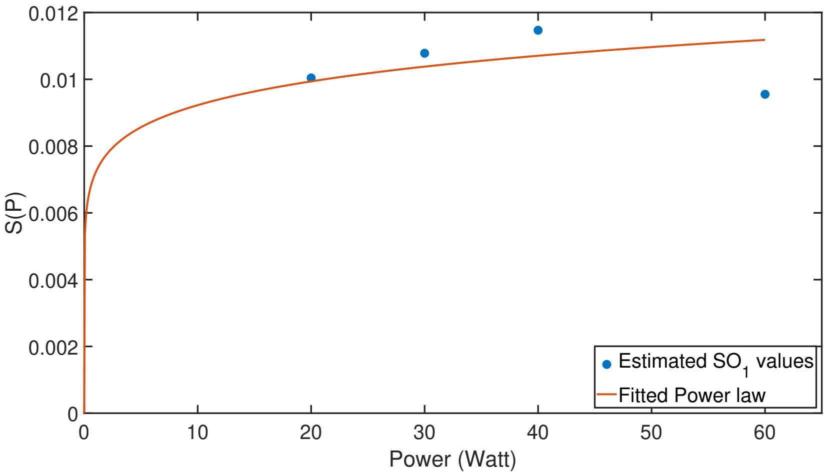

Figure 5.19: Fitting model for the kinetic parameter S1 depending on ultrasound power change.

5.3.3 Ultrasound Frequency Impact on Crystal Breakage

Another important parameter in the ultrasound experimental set-up is the frequency. The previous experiments were performed with a constant ultrasound frequency at 41 kHz. In this paragraph, two more experiments within the analysis of frequency impact are investigated. In particular, the cases of 19.5 kHz and 60.5 kHz are modeled with the CAT method, respectively. In these instances, the ultrasound power is constant at 30 W.

Figure 5.20 depicts the simulation results compared to the experimental measurements when the frequency is decreased at 19.5 kHz. The 19.5 kHz experiment still shows the same tendencies as in the 41 kHz experiments, i.e. an immediate generation of small particles. In the number density figure 5.20a the results of the simulation model are accurate enough. Especially after $t = 4320\,sec$, the algorithm can fit calculate the higher number densities with negligible deviations. In the case of the larger particles, there are some differences compared to the experimental measurements, but the results are quite satisfactory in total. The volume distribution, figure 5.20b has some common characteristics with the similar case of 41 kHz. However, according to the left top of the curve, the volume of the smaller particles is larger. Moreover, there are bigger, but fewer large particles even after $t = 5520\,sec$.

Figure 5.21 illustrates the CAT model results compared to the experimental measurements when the frequency is increased at 60.5 kHz. In the case of 60.5 kHz, the differences in the results are significant compared to the other experimental set-up instances. The main conclusion is that this frequency increase cannot produce a sufficient amount of crystals. This fact can be captured both in number and volume density distributions, shown in Figures 5.21. In the former distribution many large particles of the order of 0.5 to 1.5 μm can be observed. From the volume perspective, there is not a noticeable peak in smaller particles in Figure 5.21b, while the larger particles seem to remain unaffected. As far as the simulation model is concerned, it is difficult to approach the corresponding experimental number densities in Figure 5.21a.

In general, the cavitation bubbles formed by low frequencies reach larger sizes before exploding, resulting in more intense shock waves, hence a decrease in frequency leads to smaller diameters. In the case of 60.5 kHz, however, the increase in frequency significantly reduces the breakage effect. Higher frequencies produce smaller bubbles, resulting in weaker shock waves. Further-

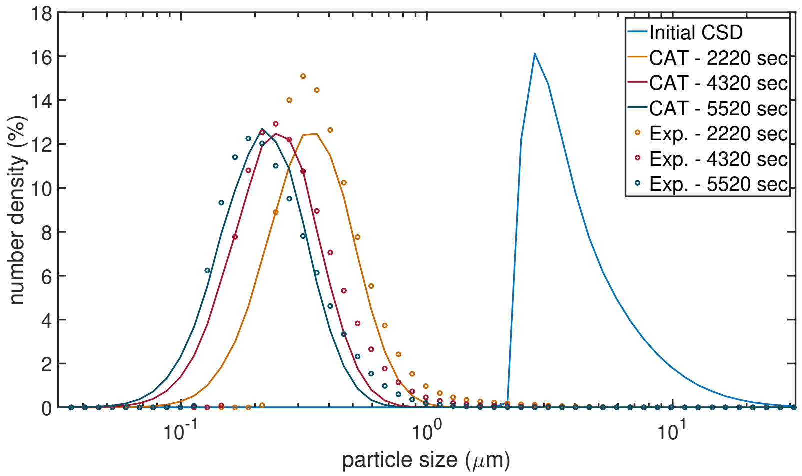

(a)

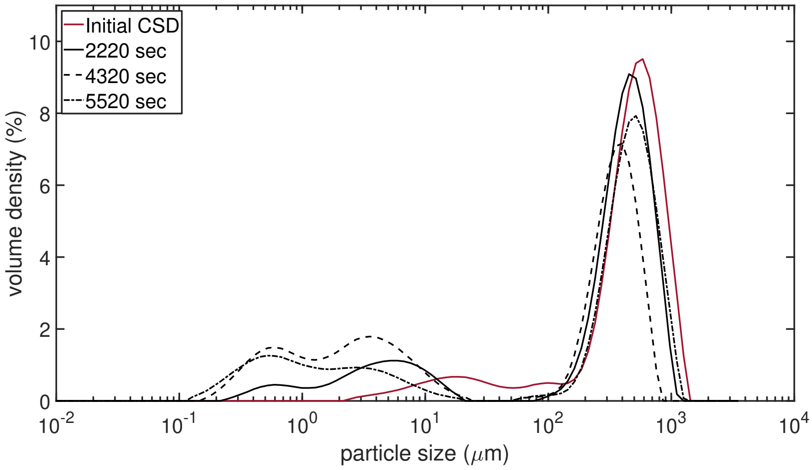

(b)

Figure 5.20: (a) Snapshots of number density distribution function and (b) The corresponding experimental volume density distribution for the 1st case of 30 W and 19.5 kHz.

more, it appears that there is a frequency cutoff below which significantly less breakage occurs, and above which increasing the frequency has no effect.

Table 9 reports the fitting of the CAT method to experimental results for the three different cases of ultrasound frequency.

Case	Power (W)	Frequency (kHz)	Kinetic Parameters S_1	m	$min\, f(x)$
1	30.0	19.5	$15.19 \cdot 10^{-3}$	0.6874	$2.6798 \cdot 10^{-3}$
2	30.0	41.0	$10.78 \cdot 10^{-3}$	0.8707	$4.3013 \cdot 10^{-3}$
3	30.0	60.5	$8.28 \cdot 10^{-3}$	1.2103	$5.9191 \cdot 10^{-3}$

Table 9: Optimization results referred to minimization of Eq. (3.72). The S_1 and m are the optimum kinetic parameters as described in Eq. (3.54). For all cases, $q = 5$.

The optimum fitting is obtained in the case of 30 W and 19.5 kHz, while on the other hand, the model of 60.5 kHz cannot manage a good adjustment to the experimental measurements.

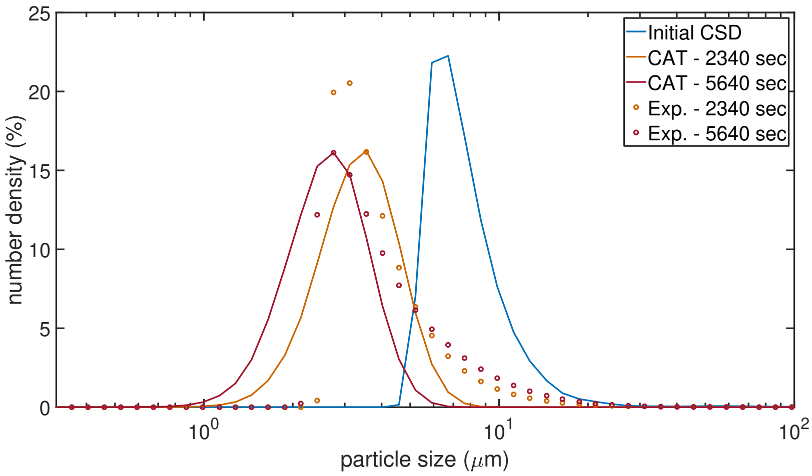

(a)

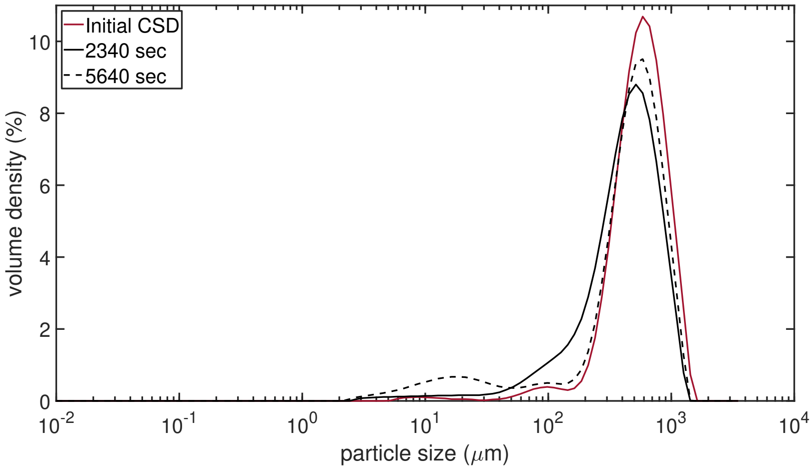

(b)

Figure 5.21: (a) Snapshots of number density distribution function and (b) The corresponding experimental volume density distribution for the 2nd case of 30 W and 60.5 kHz.

5.3.4 Comparing with L-glutamic acid

In this section, the L glutamic acid, LGLu is studied in order to verify the efficiency of the CAT method in a different compound for ultrasound crystal breakage. The ultrasound specifications concern 30 W of power and 41 kHz of frequency.

Figure 5.22a shows the number density of the produced crystals and Figure 5.22b illustrates the experimental volume density distribution, respectively. Similar tendencies as the $NaClO_3$ experiments can be observed. The formation of small particles causes a rapid decrease in mean diameter that decays over time. It is clear that the two experiments using different compounds, had a different initial distribution. Moreover, in the case of LGLu, the diameters are still larger than those of $NaClO_3$ after the same processing times.

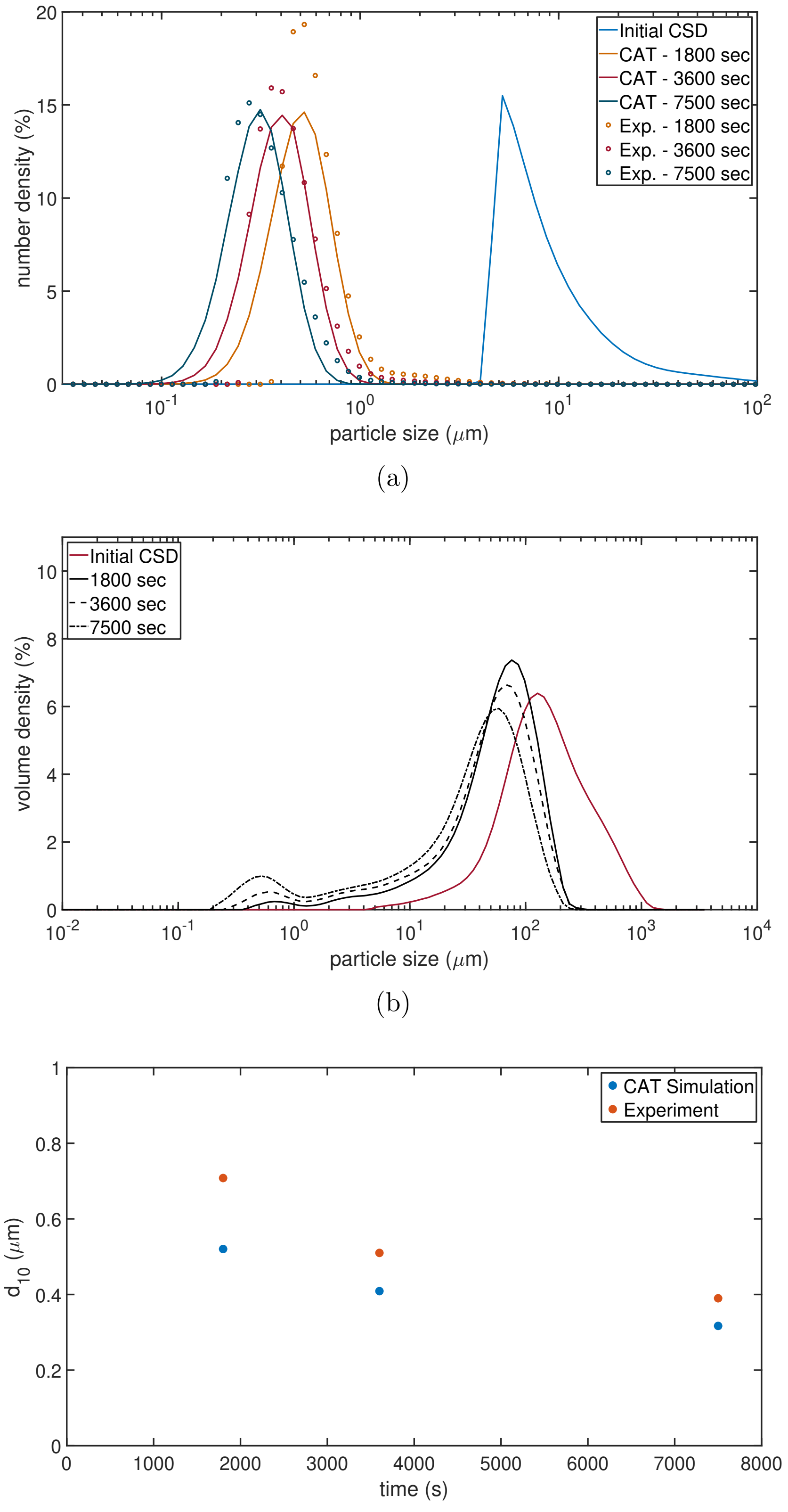

(a)

(b)

(c)

Figure 5.22: (a) Snapshots of number density distribution function, (b) The corresponding experimental volume density distribution and (c) Evolution of the mean diameter d_{10} for the case of LGLu compound in 30 W and 41 kHz.

The CAT methodology using the U-shaped model of distribution (3.70) shows similar tends at both the $NaClO_3$ and LGLu compounds. Therefore, the model can be efficient with the appropriate tuning. Comparing figures 5.17a and 5.22a for $NaClO_3$ and LGLu, respectively, the CAT simulation for the latter compound produces better results even after 125 mins of time. In the volume distribution curve, shown in Figure 5.22b appears that the breaking process of the crystals is smooth, while the volume density of the smaller particles is more negligible compared to $NaClO_3$ corresponding case. Similarly with the latter case, figure 5.22c illustrates the d_{10} diameters for the LGLu simulation. Both of the cases of the different compounds lead to smaller diameters for larger times.

Table 10 reports the fitting results of the CAT method to experimental results for the two different compounds. The optimization results for both cases are similar.

Case	Compound	Power (W)	Frequency (kHz)	Kinetic Parameters S_1	Kinetic Parameters m	$min\, f(x)$
1	$NaClO_3$	30.0	41.0	$10.78 \cdot 10^{-3}$	0.8707	$4.3013 \cdot 10^{-3}$
2	LGLu	30.0	41.0	$9.17 \cdot 10^{-3}$	0.9595	$4.1861 \cdot 10^{-3}$

Table 10: Optimization results referred to minimization of Eq. (3.72). The S_1 and m are the optimum kinetic parameters as described in the Eq. (3.54). For all these cases we consider the U-shaped distribution with $q = 5$.

6 Conclusions and Future Work

In this thesis, the cell average technique (CAT) is implemented for the numerical solution of population balance equations (PBEs) modeling the breakage mechanism. In particular, we aim to simulate ultrasound breakage experiments. These experiments took place in KU Leuven from Dr. Christos Xiouras and are referred to various ultrasound experimental set-ups. Before this application, we first validate CAT simulating breakage PBEs with analytic solutions.

An important part of this study is the specification of the suitable daughter distribution function and the relevant parameters in breakage processes. To this end, an optimization framework able to handle the system parameters has to be developed. The experimental procedure was a major part of the whole process and the different cases of experiments that were executed assisted to draw the conclusions.

Concerning the ultrasound experimental procedure, we enlist some basic observations:

- The variation in power from 20 to 60 W with constant frequency at 41 kHz, showed that increasing the power initially has a large influence on the breakage but only up to a certain wattage. The reason behind this is that increasing the power leads to more and larger cavitation bubbles up to a given point. Larger bubbles lead to more violent implosions causing more breakage. At higher power, the reactor required more cooling this indicates that the increase in power is mostly lost as heat. The effect of the increase of ultrasound power on the kinetic parameters can be represented by a power law equation.
- The influence of the frequency was studied by experiments at 19.5 kHz, 41 kHz and 60.5 kHz for a constant power of 30 W. The experiments indicate that lowering frequencies lead to higher breakage. This can be explained by the size of the cavitation bubbles. At lower frequencies, the bubbles are allowed to grow bigger and as a result, they implode much more violently. The increase in breakage with lower frequencies is initially quite large starting from higher frequencies but this effect diminishes similar to the power effect. These observations indicate that it will be difficult to reach any desired crystal size with ultrasound.
- The main compound that is studied is the $NaClO_3$, but we also study the LGLu for the set-up of 30 W of power and 41 kHz of frequency. The results for the latter compound were remarkably satisfactory.

In general, as far as the different experimental set-ups are concerned, it is difficult to completely break large crystals and produce the desired particle size.

The comparison of the different daughter distributions that are found in the literature proved that the U-shaped daughter distribution equation (3.70) yielded more accurate simulation results compared to the experimental ones. Even in cases where different experimental set-ups, depending on the ultrasound power and frequency were tested, this model presents the optimum behavior. Overall this specific CAT model for crystal breakage simulation produces satisfactory results.

The computational model can simulate the breakage mechanism. It will be interesting to investigate the approach of the CAT method in growth, nucleation and agglomeration mechanisms. The CAT method can be used for simulating different breakage systems. It can be used for glass bead grinding. In that case, a complete model simulating the four mechanisms of the

Viedma ripening model could be developed. In addition, a different model able to describe the deracemization process could be implemented.

It has been pointed out that the breakage rate and the daughter distribution functions have major importance in the crystal breakage mechanism. In this thesis, the latter function is investigated in order to fit the simulation model in the experimental measurements. The breakage rate that is used in this work is based on the generalized power law equation that is proposed in the literature for simulating ultrasound breakage. There are various approaches in case that different breakage methods are studied, which may be fitted also in our system.

Finally, a more thorough study of the optimization techniques used to fit the experimental data can be made. In this thesis, we implemented a Nelder-Mead optimization, however one can also investigate alternative methods, as for example, evolutionary optimization algorithms, simulated annealing, or particle swarms.

References

References

[1] Atul H Bari and Aniruddha B Pandit. Ultrasound-facilitated particle breakage: Estimation of kinetic parameters using population balance modelling. *The Canadian Journal of Chemical Engineering*, 92(12):2046–2052, 2014.

[2] VK Belyaev and RESHETNY. II. Effect of ultrasound on growth and dissolution of single crystals in a drop of solution, 1967.

[3] John R Blake, Giles S Keen, Robert P Tong, and Miles Wilson. Acoustic cavitation: the fluid dynamics of non–spherical bubbles. *Philosophical Transactions of the Royal Society of London. Series A: Mathematical, Physical and Engineering Sciences*, 357(1751):251–267, 1999.

[4] Christopher E Brennen. *Cavitation and bubble dynamics*. Cambridge University Press, 2014.

[5] Benjamin Caballero, Luiz C Trugo, and Paul M Finglas. *Encyclopedia of food sciences and nutrition*. Academic, 2003.

[6] Peter W Cains, Peter D Martin, and Christopher J Price. The use of ultrasound in industrial chemical synthesis and crystallization. 1. applications to synthetic chemistry. *Organic process research & development*, 2(1):34–48, 1998.

[7] Laura de los Santos Castillo-Peinado and María Dolores Luque de Castro. The role of ultrasound in pharmaceutical production: sonocrystallization. *Journal of Pharmacy & Pharmacology*, 68(10):1249–1267, 2016.

[8] RB Diemer and JH Olson. A moment methodology for coagulation and breakage problems: Part 3—generalized daughter distribution functions. *Chemical Engineering Science*, 57(19):4187–4198, 2002.

[9] J Dooher, Robert Lippman, Terry Morrone, Hugh Pohle, and Donald Wright. Ultrasonic disintigration of particles. In *1977 Ultrasonics Symposium*, pages 11–16. IEEE, 1977.

[10] Akinola Falola, Antonia Borissova, and Xue Zhong Wang. Extended method of moment for general population balance models including size dependent growth rate, aggregation and breakage kernels. *Computers & chemical engineering*, 56:1–11, 2013.

[11] Antonios A Fytopoulos, Michail E Kavousanakis, Tom Van Gerven, Andreas G Boudouvis, Georgios D Stefanidis, and Christos Xiouras. Crystal growth, dissolution, and agglomeration kinetics of sodium chlorate. *Industrial & Engineering Chemistry Research*, 60(19):7367–7384, 2021.

[12] Zdeněk Grof, Carl M Schoellhammer, Pavol Rajniak, and František Štěpánek. Computational and experimental investigation of needle-shaped crystal breakage. *International journal of pharmaceutics*, 407(1-2):12–20, 2011.

[13] Z Guo, M Zhang, H Li, J Wang, and E Kougoulos. Effect of ultrasound on anti-solvent crystallization process. *Journal of Crystal Growth*, 273(3-4):555–563, 2005.

[14] Zhichao Guo, Alan G Jones, and Ningning Li. The effect of ultrasound on the homogeneous nucleation of baso4 during reactive crystallization. *Chemical engineering science*, 61(5):1617–1626, 2006.

[15] Richard W Hartel. Advances in food crystallization. *Annual review of food science & technology*, 4:277–292, 2013.

[16] Frank Hoffmann. *Introduction to crystallography.* Springer Nature, 2020.

[17] Hugh M Hulburt and Stanley Katz. Some problems in particle technology: A statistical mechanical formulation. *Chemical engineering science*, 19(8):555–574, 1964.

[18] Martin Iggland and Marco Mazzotti. A population balance model for chiral resolution via viedma ripening. *Crystal growth & design*, 11(10):4611–4622, 2011.

[19] Alexander P Kapustin. *The effects of ultrasound on the kinetics of crystallization.* Springer Science & Business Media, 2012.

[20] Margaritis Kostoglou. Extended cell average technique for the solution of coagulation equation. *Journal of colloid and interface science*, 306(1):72–81, 2007.

[21] HJ Kramer, G van Rosmalen, and J ter Hosrt. Basic process design for crystallization processes. *Delft University of Technology, Delft, The Netherlands*, 2003.

[22] J Kumar, G Warnecke, M Peglow, and S Heinrich. Comparison of numerical methods for solving population balance equations incorporating aggregation and breakage. *Powder Technology*, 189(2):218–229, 2009.

[23] Jitendra Kumar. Numerical approximations of population balance equations in particulate systems. 2007.

[24] Jitendra Kumar, Mirko Peglow, Gerald Warnecke, and Stefan Heinrich. An efficient numerical technique for solving population balance equation involving aggregation, breakage, growth and nucleation. *Powder Technology*, 182(1):81–104, 2008.

[25] Sanjeev Kumar and Doraiswami Ramkrishna. On the solution of population balance equations by discretization—i. a fixed pivot technique. *Chemical Engineering Science*, 51(8):1311–1332, 1996.

[26] Masahiro Kurotani, Etsuko Miyasaka, Satomi Ebihara, and Izumi Hirasawa. Effect of ultrasonic irradiation on the behavior of primary nucleation of amino acids in supersaturated solutions. *Journal of crystal growth*, 311(9):2714–2721, 2009.

[27] Karl A Kusters, Sotiris E Pratsinis, Steven G Thoma, and Douglas M Smith. Ultrasonic fragmentation of agglomerate powders. *Chemical engineering science*, 48(24):4119–4127, 1993.

[28] Werner Lauterborn and Alfred Vogel. Modern optical techniques in fluid mechanics. *Annual Review of Fluid Mechanics*, 16(1):223–244, 1984.

[29] Alfred Y Lee and Allan S Myerson. Particle engineering: Fundamentals of particle formation and crystal growth. *MRS bulletin*, 31(11):881–886, 2006.

[30] Stephanie S Lee, Chang Su Kim, Enrique D Gomez, Balaji Purushothaman, Michael F Toney, Cheng Wang, Alexander Hexemer, John E Anthony, and Yueh-Lin Loo. Controlling

nucleation and crystallization in solution-processed organic semiconductors for thin-film transistors. *Advanced Materials*, 21(35):3605–3609, 2009.

[31] TG Leighton. The acoustic bubble.| academic. *Press, London*, pages 234–243, 1994.

[32] Alison Lewis, Marcelo Seckler, Herman Kramer, and Gerda Van Rosmalen. *Industrial crystallization: fundamentals and applications*. Cambridge University Press, 2015.

[33] Hong Li, Jingkang Wang, Ying Bao, Zhichao Guo, and Muyan Zhang. Rapid sonocrystallization in the salting-out process. *Journal of crystal growth*, 247(1-2):192–198, 2003.

[34] Po-Wei Liang, Chien-Yi Liao, Chu-Chen Chueh, Fan Zuo, Spencer T Williams, Xu-Kai Xin, Jiangjen Lin, and Alex K-Y Jen. Additive enhanced crystallization of solution-processed perovskite for highly efficient planar-heterojunction solar cells. *Advanced materials*, 26(22):3748–3754, 2014.

[35] Yulan Lin, Kangtaek Lee, and Themis Matsoukas. Solution of the population balance equation using constant-number monte carlo. *Chemical Engineering Science*, 57(12):2241–2252, 2002.

[36] Alan W Mahoney, Francis J Doyle III, and Doraiswami Ramkrishna. Inverse problems in population balances: growth and nucleation from dynamic data. *AIChE journal*, 48(5):981–990, 2002.

[37] Ivan Vesselinov Markov. *Crystal growth for beginners: fundamentals of nucleation, crystal growth and epitaxy*. World scientific, 2016.

[38] Alan D McNaught, Andrew Wilkinson, et al. *Compendium of chemical terminology*, volume 1669. Blackwell Science Oxford, 1997.

[39] Alexander McPherson. Introduction to protein crystallization. *Methods*, 34(3):254–265, 2004.

[40] CJ Meyer and DA Deglon. Particle collision modeling–a review. *Minerals Engineering*, 24(8):719–730, 2011.

[41] JW Mullin. 8—industrial techniques and equipment. *Crystallization, 4th ed.; Mullin, JW, Ed.; Butterworth-Heinemann: Oxford, UK*, pages 315–402, 2001.

[42] John A Nelder and Roger Mead. A simplex method for function minimization. *The computer journal*, 7(4):308–313, 1965.

[43] Wim L Noorduin, Toshiko Izumi, Alessia Millemaggi, Michel Leeman, Hugo Meekes, Willem JP Van Enckevort, Richard M Kellogg, Bernard Kaptein, Elias Vlieg, and Donna G Blackmond. Emergence of a single solid chiral state from a nearly racemic amino acid derivative. *Journal of the American Chemical Society*, 130(4):1158–1159, 2008.

[44] LG POLOTSKY, DY OVSIYENKO, ZL Khodov, and YG Sosnina. Effect of an ultrasound on the perfection of melt- grown aluminium single crystals. *PHYS METALS METALLOGR, 1966, 21,–5–, 81-84*, 1966.

[45] F Pratola, SJR Simons, and AG Jones. A novel experimental device for measurement of agglomerative crystallization forces. *Chemical Engineering Research and Design*, 80(5):441–448, 2002.

[46] Doraiswami Ramkrishna. *Population balances: Theory and applications to particulate systems in engineering.* Elsevier, 2000.

[47] Michael L Rasche, Brad W Zeiger, Kenneth S Suslick, and Richard D Braatz. Mathematical modelling of the evolution of the particle size distribution during ultrasound-induced breakage of aspirin crystals. *Chemical Engineering Research and Design*, 132:170–177, 2018.

[48] Åke C Rasmuson. Introduction to crystallization of fine chemicals and pharmaceuticals. In *Molecules: Nucleation, Aggregation and Crystallization: Beyond Medical and Other Implications*, pages 145–172. World Scientific, 2009.

[49] William T Richards and Alfred L Loomis. The chemical effects of high frequency sound waves i. a preliminary survey. *Journal of the American Chemical Society*, 49(12):3086–3100, 1927.

[50] Graham Ruecroft, David Hipkiss, Tuan Ly, Neil Maxted, and Peter W Cains. Sonocrystallization: the use of ultrasound for improved industrial crystallization. *Organic Process Research & Development*, 9(6):923–932, 2005.

[51] Mehakpreet Singh, Jitendra Kumar, Andreas Bück, and Evangelos Tsotsas. A volume-consistent discrete formulation of aggregation population balance equations. *Mathematical Methods in the Applied Sciences*, 39(9):2275–2286, 2016.

[52] MG Sirotyuk. Experimental investigations of ultrasonic cavitation. In *High-Intensity Ultrasonic Fields*, pages 261–343. Springer, 1971.

[53] Leyla-Cann Sögütoglu, René RE Steendam, Hugo Meekes, Elias Vlieg, and Floris PJT Rutjes. Viedma ripening: a reliable crystallisation method to reach single chirality. *Chemical Society Reviews*, 44(19):6723–6732, 2015.

[54] Rene RE Steendam, Maxime CT Brouwer, Evelien ME Huijs, Michael W Kulka, Hugo Meekes, Willem JP van Enckevort, Jan Raap, Floris PJT Rutjes, and Elias Vlieg. Enantiopure isoindolinones through viedma ripening. *Chemistry–A European Journal*, 20(42):13527–13530, 2014.

[55] Rene RE Steendam, Bram Harmsen, Hugo Meekes, Willem JP Van Enckevort, Bernard Kaptein, Richard M Kellogg, Jan Raap, Floris PJT Rutjes, and Elias Vlieg. Controlling the effect of chiral impurities on viedma ripening. *Crystal growth & design*, 13(11):4776–4780, 2013.

[56] Kenneth S Suslick. The chemical effects of ultrasound. *Scientific American*, 260(2):80–87, 1989.

[57] Kenneth S Suslick. Sonochemistry. *science*, 247(4949):1439–1445, 1990.

[58] Kenneth Sanders Suslick. *Ultrasound: its chemical, physical, and biological effects.* VCH Publishers, 1988.

[59] P Synowiec, AG Jones, and P Ayazi Shamlou. Crystal break-up in dilute turbulently agitated suspensions. *Chemical engineering science*, 48(20):3485–3495, 1993.

[60] Makio Uwaha. Simple models for chirality conversion of crystals and molecules by grinding. *Journal of the Physical Society of Japan*, 77(8):083802–083802, 2008.

[61] Maarten W van der Meijden, Michel Leeman, Edith Gelens, Wim L Noorduin, Hugo Meekes, Willem JP van Enckevort, Bernard Kaptein, Elias Vlieg, and Richard M Kellogg. Attrition-enhanced deracemization in the synthesis of clopidogrel-a practical application of a new discovery. *Organic Process Research and Development*, 13(6):1195–1198, 2009.

[62] BP Vasilev and KN Vinogradov. Amplification of high-intensity ultrasound in cadmium sulfide single crystals. *SOVIET PHYS SOLID STATE, NOV. 1967, 9,-5-, 1052-1054*, 1967.

[63] Cristobal Viedma. Experimental evidence of chiral symmetry breaking in crystallization from primary nucleation. *Journal of Crystal growth*, 261(1):118–121, 2004.

[64] Cristobal Viedma. Chiral symmetry breaking during crystallization: complete chiral purity induced by nonlinear autocatalysis and recycling. *Physical review letters*, 94(6):065504, 2005.

[65] Tiefeng Wang and Jinfu Wang. Numerical simulations of gas–liquid mass transfer in bubble columns with a cfd–pbm coupled model. *Chemical engineering science*, 62(24):7107–7118, 2007.

[66] Patrick Wilmink, Celine Rougeot, Klaus Wurst, Morgane Sanselme, Maarten van der Meijden, Wojciech Saletra, Gerard Coquerel, and Richard M Kellogg. Attrition induced deracemisation of 2-fluorophenylglycine. *Organic Process Research and Development*, 19(1):302–308, 2015.

[67] Janusz A Wójcik and Alan G Jones. Dynamics and stability of continuous msmpr agglomerative precipitation: numerical analysis of the dual particle coordinate model. *Computers & chemical engineering*, 22(4-5):535–545, 1998.

[68] Christos Xiouras, Antonios A Fytopoulos, Joop H Ter Horst, Andreas G Boudouvis, Tom Van Gerven, and Georgios D Stefanidis. Particle breakage kinetics and mechanisms in attrition-enhanced deracemization. *Crystal Growth & Design*, 18(5):3051–3061, 2018.

[69] Christos Xiouras, Joop H Ter Horst, Tom Van Gerven, and Georgios D Stefanidis. Coupling viedma ripening with racemic crystal transformations: mechanism of deracemization. *Crystal Growth and Design*, 17(9):4965–4976, 2017.

[70] Christos Xiouras, Jasper Van Aeken, Joris Panis, Joop H Ter Horst, Tom Van Gerven, and Georgios D Stefanidis. Attrition-enhanced deracemization of naclo3: Comparison between ultrasonic and abrasive grinding. *Crystal Growth & Design*, 15(11):5476–5484, 2015.

[71] Robert M Ziff. New solutions to the fragmentation equation. *Journal of Physics A: Mathematical and General*, 24(12):2821, 1991.